AD-A060 381 OHIO STATE UNIV RESEARCH FOUNDATION COLUMBUS F/G 5/1
EPITAXIAL MAGNETIC FILM EVALUATION TECHNIQUES.(U)
MAY 78 P E WIGEN, K J BREEDING F33615-77-C-1002
UNCLASSIFIED OSURF-MPN-764596 AFAL-TR-78-67 NL

1 OF 1
AD
A060381

END
DATE
FILMED
1-79
DDC

② LEVEL II

AFAL-TR-78-67

2

EXPITAXIAL MAGNETIC FILM EVALUATION TECHNIQUES

Philip E. Wigen, Department of Physics
Kenneth J. Breeding, Department of Electrical Engineering

The Ohio State University
Columbus, Ohio 43210

MAY 1978

Interim Report November 1976 - October 1977

Approved for public release; distribution unlimited.

AIR FORCE AVIONICS LABORATORY
AIR FORCE WRIGHT AERONAUTICAL LABORATORIES
AIR FORCE SYSTEMS COMMAND
WRIGHT-PATTERSON AIR FORCE BASE, OHIO 45433

AFAL-TR-78-67

NOTICE

This report has been reviewed by the Information Office (OI) and is releasable to the National Technical Information Service (NTIS). At NTIS it will be available to the general public, including foreign nations.

This technical report has been reviewed and is approved for publication.

Millard G. Mier

MILLARD G. MIER
Project Engineer

FOR THE COMMANDER

Robert D Larson

ROBERT D. LARSON, Chief
Electronic Research Branch
Electronic Technology Div.
AF Avionics Laboratory

AIR FORCE/56780/24 July 1978 — 175

1

UNCLASSIFIED

SECURITY CLASSIFICATION OF THIS PAGE (When Data Entered)

⑱ ⑲ REPORT DOCUMENTATION PAGE

READ INSTRUCTIONS BEFORE COMPLETING FORM

1. REPORT NUMBER AFAL-TR-78-67	2. GOVT ACCESSION NO.	3. RECIPIENT'S CATALOG NUMBER
4. TITLE (and Subtitle) ⑥ EPITAXIAL MAGNETIC FILM EVALUATION TECHNIQUES.		5. TYPE OF REPORT & PERIOD COVERED Technical Nov. 1, 1976 - Oct. 31, 1977
		6. PERFORMING ORG. REPORT NUMBER MPN 764596
7. AUTHOR(s) P.E. Wigen and K.J. Breeding		8. CONTRACT OR GRANT NUMBER(s) ⑮ F33615-77-C-1002
9. PERFORMING ORGANIZATION NAME AND ADDRESS OSU Research Foundation 1314 Kinnear Road Columbus, OH 43212 61102F		10. PROGRAM ELEMENT, PROJECT, TASK AREA & WORK UNIT NUMBERS ⑯ 2305-R2-70 ⑰ R2
11. CONTROLLING OFFICE NAME AND ADDRESS AIR FORCE AVIONICS LABORATORY (DHR) WRIGHT-PATTERSON AIR FORCE BASE, OHIO		12. REPORT DATE ⑪ MAY 1978
		13. NUMBER OF PAGES 59
14. MONITORING AGENCY NAME & ADDRESS (if different from Controlling Office) ⑩ Philip E. /Wigen, Kenneth J. /Breeding		15. SECURITY CLASS. (of this report) Unclassified
		15a. DECLASSIFICATION/DOWNGRADING SCHEDULE

16. DISTRIBUTION STATEMENT (of this Report)

Approved for public release; distribution unlimited.

⑫ 68p.

17. DISTRIBUTION STATEMENT (of the abstract entered in Block 20, if different from Report)

⑨ Interim rept. 1 Nov 76-31 Oct 77,

DDC
RECEIVED
OCT 26 1978
B

18. SUPPLEMENTARY NOTES

⑭ OSURF-MPN-764596

19. KEY WORDS (Continue on reverse side if necessary and identify by block number)

Magnetic Bubbles, Garnet Films, M-H Looper, Ferromagnetic Resonance, Spinwave Resonance Image matching, Optical Waveguide, Faraday Rotation, Optical positioning, Moment Invariance

20. ABSTRACT (Continue on reverse side if necessary and identify by block number)

This annual report reviews the progress of the first year in establishing experimental programs at three different locations and initiating research programs. At the Avionics Laboratory a new research laboratory was developed, a ferromagnetic resonance spectrometer for making whole wafer measurements was built and tested and the components of a M-H looper operating at 200Hz and sweeping $H_{(max)} = \pm$ 400 Oe. was built. Construction details of these devices are

+ or − (Over)

DD FORM 1 JAN 73 1473 EDITION OF 1 NOV 65 IS OBSOLETE

UNCLASSIFIED

SECURITY CLASSIFICATION OF THIS PAGE (When Data Entered)

267 360

20. abstract (cont.)

described in this report. At the OSU Physics department, a ~~new~~ experimental program was initiated to ~~experimentally~~ investigate the scattering of spinwaves from domain walls at microwave frequencies. A ~~new~~ experimental program investigating the response of domain walls to rf frequencies was also initiated. A theoretical progress report of spinwave scattering is also included. At the OSU Electrical Engineering department, the initial phases of an add on a~~d~~mendment to the contract to investigate the feasibility of testing and characterizing very large (10^9 and above) memories is reported. The thrust of this effort will include a scanning of the bubble memory overlay pattern and an electrical characterization process using polarized laser light coupled to an optical wave guide. The presence of the magnetic bubble will introduce a change in the faraday rotation of the plane of polarization. This will be used as the "Bubble detector" in a parallel access characterization process.

10 to the 9th power

PREFACE

This technical report covers the research performed under Contract No. F33615-77-C-1002 from 1 October 1976 to 30 September 1977.

The contract is with the Physics Department with Professor P. E. Wigen as co-principal investigator and the Electrical Engineering Department with Professor K. J. Breeding as co-principal investigator. Both departments are located at The Ohio State University. The thrust of the work was Epitaxial Magnetic Film Evaluation Techniques, and is conducted under the direction of Dr. Millard Mier, AFAL/DHR, Avionics Laboratory, Wright-Patterson Air Force Base, Ohio.

J. P. Omaggio and M. P. Globe were involved in this program at the Avionics Laboratory, A. A. Parker and P. Lemaye were involved in this program at the Physics Department, OSU and H. K. Brown and R. Thienlikit were involved in this program at the Electrical Engineering Department, OSU.

TABLE OF CONTENTS

LIST OF ILLUSTRATIONS

LIST OF ILLUSTRATIONS (cont'd)

SECTION I

MATERIALS RESEARCH

3

A. Avionics Laboratory

1. M-H Looper

The characterization of the static properties of a magnetic bubble material traditionally consists of three parameters, the film thickness, h, the stripewidth W, at zero applied field and the bubble collapse field, H . All other static parameters can be calculated from these three terms. These include the saturation magnetization, the domain wall energy, characteristics length and others. Ordinarily, the stripewidth and collapse field measurements are done optically with a microscope. As bubble sizes decrease, the difficulty in these measurements increases.

The measurement of the hysteresis loop of a magnetic material provides an alternative method for obtaining material parameters. In the hysteresis loop the initial susceptibility $\chi_0 \equiv (dM/dH)_{m=o}$ and stripe collapse field are quantities measured.

From the stripe domain stability conditions developed by Kooy and Enz[1], the relationship between the film magnetization and the applied magnetic field is given as:

$$\frac{4\pi M-H}{4\pi M_s} + \frac{2\sqrt{\mu}}{1+\sqrt{\mu}} \frac{1}{\pi^2\alpha} \sum_{n=1}^{\infty} \frac{1}{n^2} \sin \pi n \left(1+\frac{M}{M_s}\right) \left[1-\exp\left(-2\pi n\alpha\right)\right] = 0 \qquad (1)$$

where M is the net magnetization of the film, M_s is the saturation magnetization, H is the applied field, h is the film thickness, $\mu \equiv 1 + 2\pi M_s^2/K_u$, $\alpha \equiv h\sqrt{\mu} \,/\, (d_1+d_2)$, d_1 is the stripe width for domains with $\vec{M}$ in the direction of H and d_2 is for domains with $\vec{M}$ in the opposite direction. This equation assumes a film of infinite area with straight domains. The domain wall energy can be related to the magnetization by the equation;

$$\frac{\sigma_W}{(4M_s)^2 h\sqrt{\mu}} \quad \frac{1+\sqrt{\mu}}{2\sqrt{\mu}} = \frac{1}{4\pi^2\alpha^2} \sum_{n=1}^{\infty} \frac{1}{n^3} \sin^2 \left[\frac{n\pi}{2}\left(1-\frac{M}{M_s}\right)\right] X \qquad (2)$$

$$\left[1-(1+2\pi n\alpha)\exp(-2\pi n\alpha)\right]$$

If the uniaxial anistropy field is large compared to $4\pi M_s$ and $\mu=1$, the above equations reduced to,[2]

$$\frac{4\pi M-H}{4\pi M_S} + \frac{d}{\pi^2 h}\sum_{n=1}^{\infty}\frac{1}{n^2}\sin\left[n\pi\left(1+\frac{M}{M_S}\right)\right]\left[1-\exp\left(\frac{-2\pi nh}{d}\right)\right] = 0 \qquad (3)$$

and

$$\frac{\lambda}{h} = \frac{d^2}{\pi^3 h^2}\sum_{n=1}^{\infty}\frac{\sin^2\left[\left(\frac{n\pi}{2}\right)\left(1-\frac{M}{M_S}\right)\right]}{n^3}\left[1-\exp\left(\frac{-2n\pi h}{d}\right)\times\left(1+\frac{2n\pi h}{d}\right)\right] \qquad (4)$$

where $d \equiv d_1 + d_2$ and λ is the material length length ($\equiv \sigma_w/4\pi M_S^2$). From equ. 3 the initial susceptibility is calculated

$$4\pi\chi_0 = \frac{1}{1+\frac{2W}{\pi h}\sum_{n=1}^{\infty}\frac{1}{n}(-1)^n\left[1-\exp\left(\frac{-\pi nh}{W}\right)\right]} \qquad (5)$$

where $W \equiv d/_2$ The relation between χ_0 and W/h can be graphed or tabulated and if χ_0 is measured W/h can be determined.[2] Similarly, using equ. 4, χ_0 and λ/h can be related. Using Thiele's conditions for bubble stability,[3] graphs of $4\pi M_S$ againist stripe collapse field can be drawn. If an independent measurement of h is made, W and $4\pi M_S$ are determined.

A typical hysterisis loop for a 2μm magnetic bubble material from Texas Instruments appears is Figure 1. This loop was obtained from a vibrating sample magnetometer with a appled field perpendicular to the film plane. The constant slope after saturation is due to the paramagnetic Gadilinium Gallium Garnet substrate, the susceptibility of which serves as a standard for calibration. The slight increase in slope just before saturation (about 200 grams) is caused by stripe collapse.

The looper used by Maartense et. al[4]. displays a derivative of the hysterisis loop. A typical loop$_3$derivative appears in Figure 2. The constant susceptibility of G^3 acts as a calibration as an offset horizontal line after saturation.

The hysterisis loop of a hypotheical ferromagnetic material appears in Figure 3. The basic loop ABCD occurs only if the applied field is raised monotonically to saturation in one direction and then reversed producing a complete cycle. If however, the field is

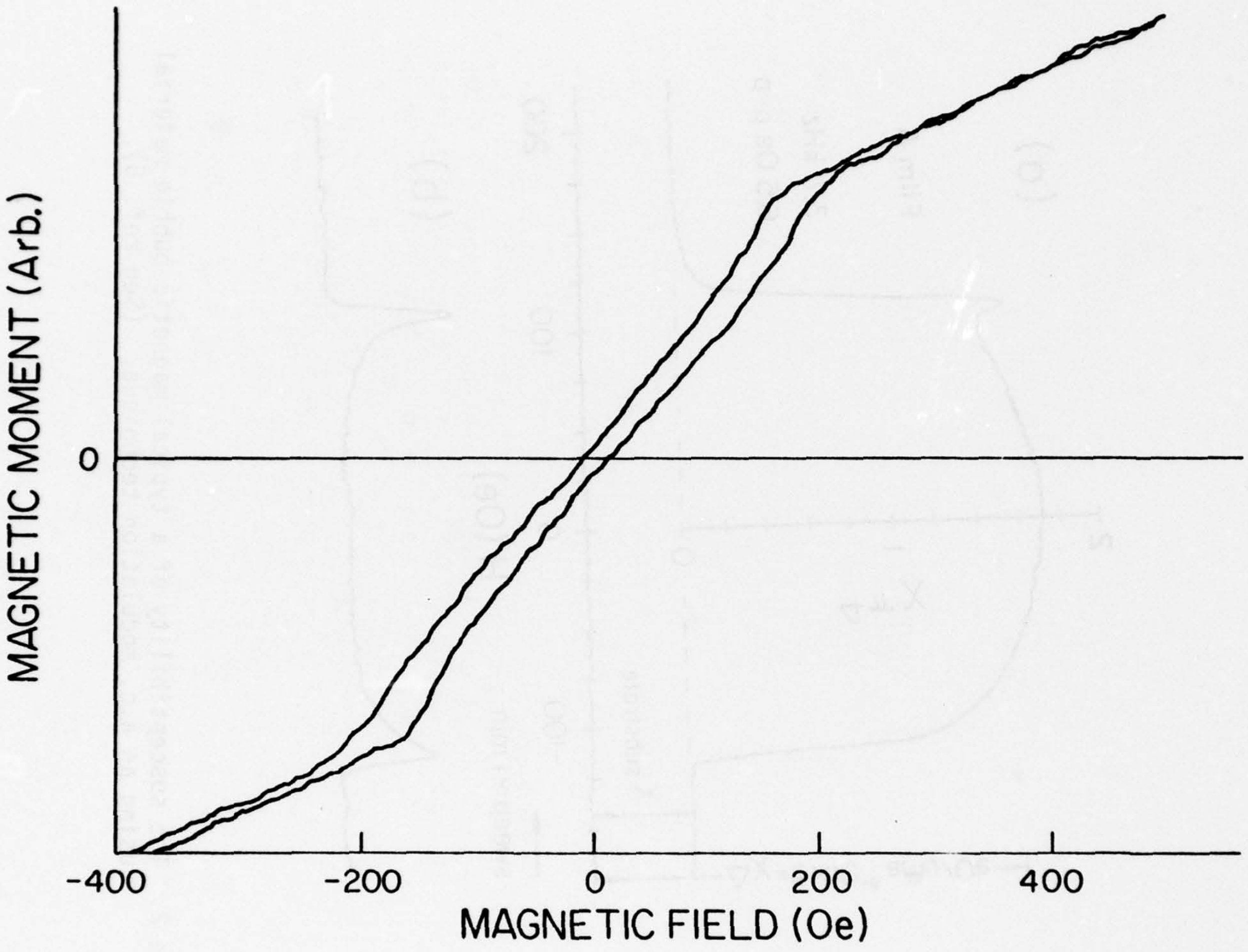

Figure 1. Hysteresis loop of a typical magnetic bubble material.

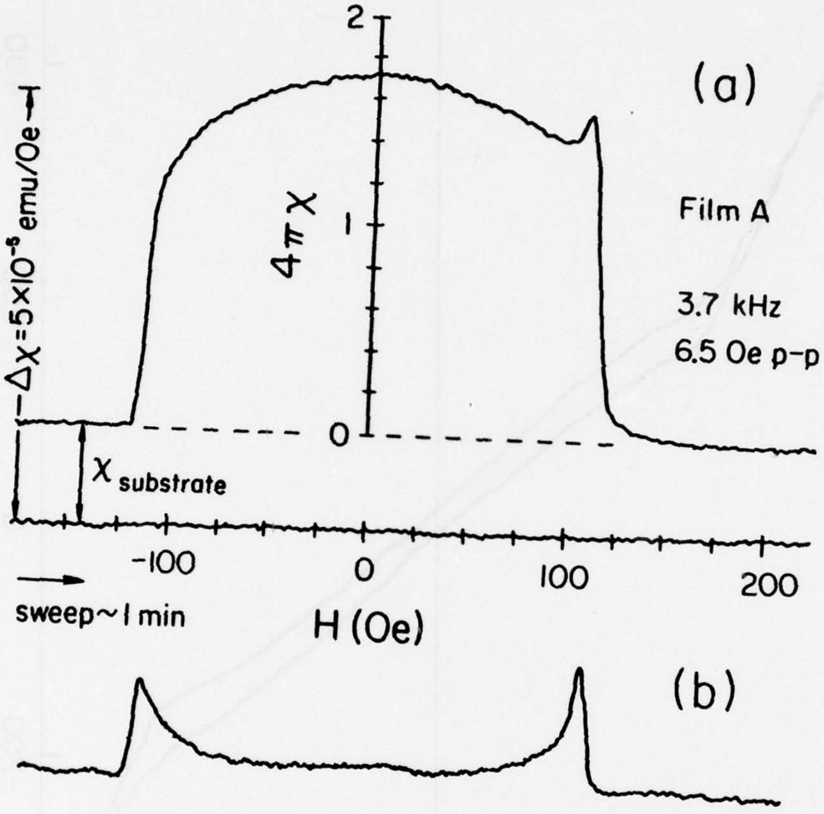

Figure 2. The susceptibility of a typical magnetic bubble material using an a.c. modulation technique. (See ref. 5).

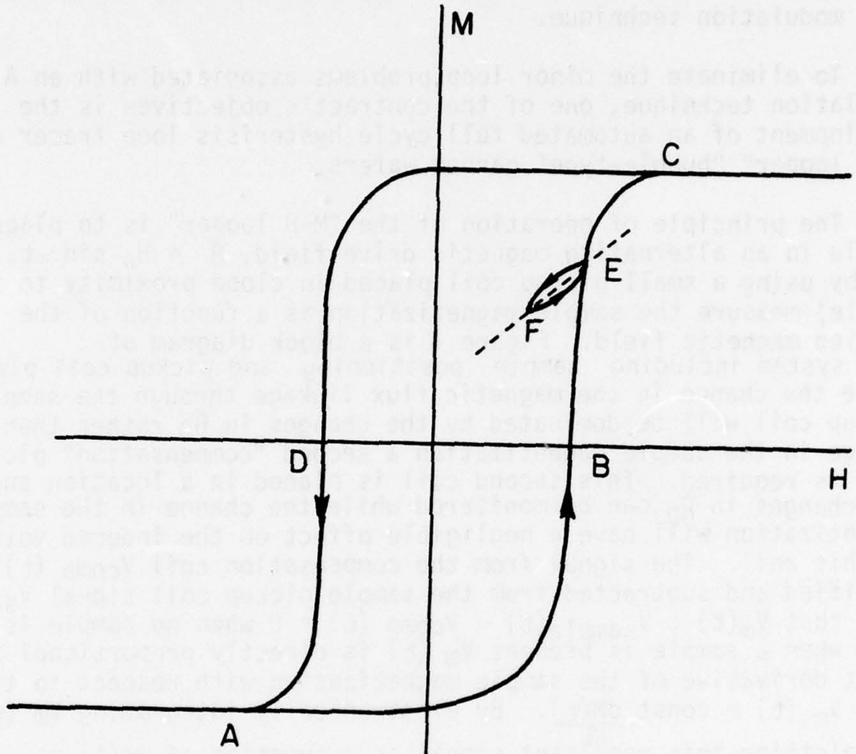

Figure 3. Hypothetical hysteresis loop for a typical magnetic material.

stopped at point E and reversed, the magnetization will not retrace its original path.[5] If the D.C. field is kept at E and a small D.C. field is imposed, the magnetization will oscillate along EFE. Some hysteresis devices[4] employ a variable D.C. field with a small A.C. component. The strength of the signal is proportional to the slope of EFE and the magnetude of the signal will be consistantly low. The extent of the error will depend on the coercivity of the material.

The M-H looper built in this laboratory oscillates through the full cycle to eliminate the minor loop problems associated with an A.C. modulation technique.

To eliminate the minor loop problems associated with an A.C. modulation technique, one of the contract's objectives is the development of an automated full cycle hysterisis loop tracer or "M-H looper" "bubble-type" garnet wafers.

The principle of operation of the "M-H looper" is to place a sample in an alternating magnetic drive field, $\vec{H} = H_0 \sin \omega t$, and by using a small pickup coil placed in close proximity to the sample, measure the sample magnetization as a function of the applied magnetic field. Figure 4 is a block diagram of this system including sample positioning and pickup coil placement Since the change in the magnetic flux linkage through the sample pickup coil will be dominated by the changes in $\vec{H}_D$ rather than the change in the sample magnetization a second "compensation" pickup coil is required. This second coil is placed in a location such that the changes in $\vec{H}_D$ can be monitered while the change in the sample magnetization will have a negligible effect on the induced voltages in this coil. The signal from the compensation coil $V_{comp}(t)$ is amplified and subtracted from the sample pickup coil signal $V_{sample}(t)$ such that $V_m(t) \equiv V_{sample}(t) - V_{comp}(t) = 0$ when no sample is present. Thus when a sample is present $V_m(t)$ is directly proportional to the first derivative of the sample magnetization with respect to time, i.e. $V_m(t) = \text{const} \frac{dM(t)}{dt}$. By electronically integrating $V_m(t)$, and plotting this resultant signal as a function of $H_D(t)$ a hysterisis loop curve is obtained for the sample. This system can then be calibrated by the use of known standard samples.

A large portion of the first year has been spent developing the basic subsystems for a non-automated prototype device shown in Figure 5. This system should be fully operational in the near future. The major subsystems constructed during this year are: the applied magnetic field drive coils, the sample holder assembly, signal pickup and compensation coils, and system electronics. Some design factors are included in the Appendix I.

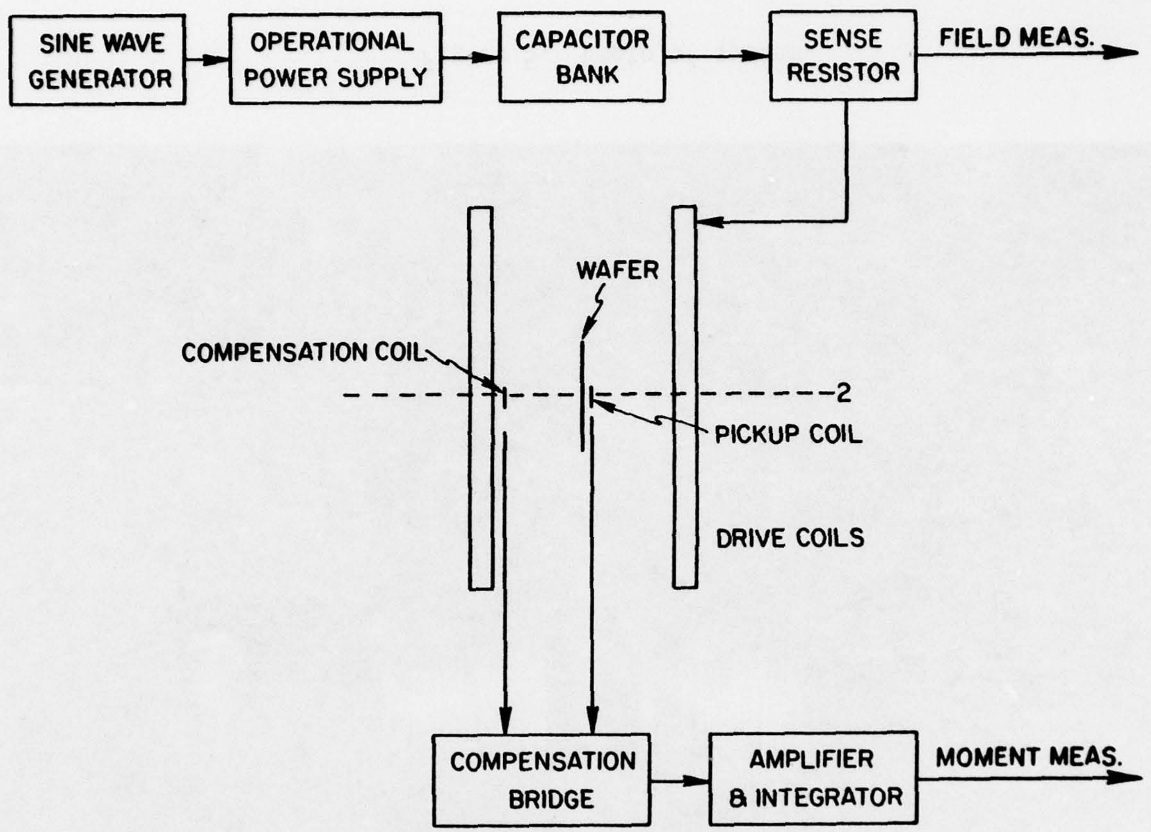

Figure 4. Block diagram of MH looper.

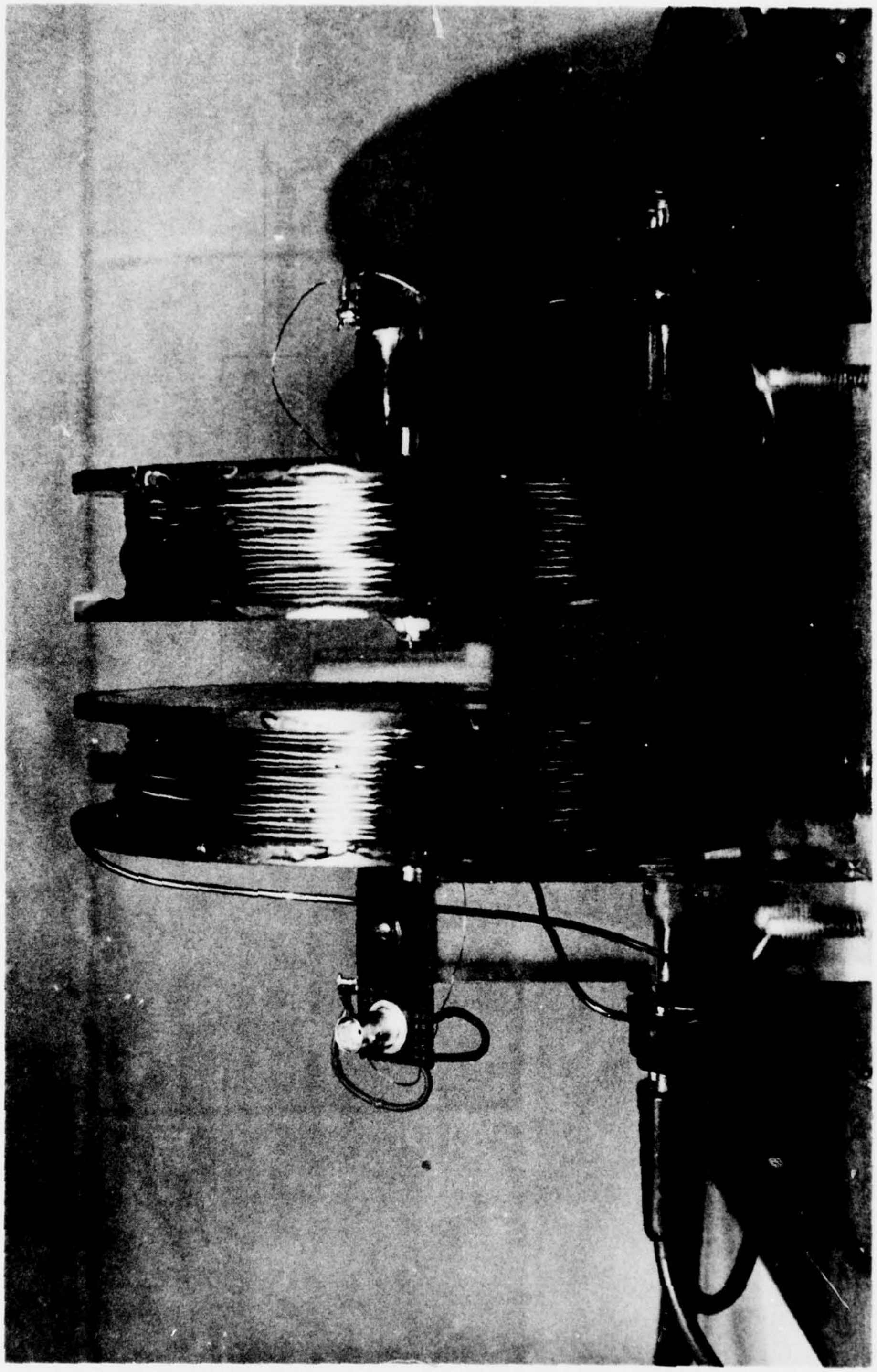

Figure 5. Photo of system.

a. Drive coils

In order to obtain the complete hysterisis curve of a ferromagnetic sample, a reversable magnetic field with sufficient intensity to magnetically saturate the sample is required. For typical bubble material films, $H_{collapse}$ is on the order of 200 gauss thus it is desired to have a maximum field intensity of at least 400 gauss. Furthermore, it is desireable that the applied magnetic field be very homogenous. The required AC magnetic field is produced by driving a set of Helmholtz coils with a Kepco 15-20 M bipolor operational amplifier power supply. The coils have 300 turns of # 14 gauge copper wire and are potted with stycast # 1266 heat conducting epoxy to help eliminate vibration within the coils. A photograph of the drive coils is shown in Figure 6. Further design consideration are included in appendix I.

In the actual installation the drive coils form part of a tuned series RLC circuit. The impedance of this circuit is given by: $|Z| = \{R^2 + (\omega L - 1/\omega C)^2\}^{1/2}$ where ω is the radical frequency of the drive field, L is the inductance of the coils, and C is the value of the tuning capacitors. For operation at 280 Hz, the minimum impedance occurs for a capacitance of approximately 70 μf. In order to facillitate tuning and to allow for operation over a range of frequencies, a capacitance bank consisting of switch selectable parallel capacitors has also been constructed.

The current through the coils, and thus the AC magnetic field, is monitered by the AC voltage drop across a 100W, 0.025Ω, 1% current shunt connected in series with the coils. The current to magnetic field strength calibration was then performed under DC conditions using a Hall effect gaussmeter. The results of this calibration and the AC characteristics of these coils are given in Tables I and II respectively. While the homogeniety of these coils was not measured experimentally, a program, included in appendix I, was written for a H-P 9820 calculator . The result indicates that field inhomogenieties should be less than 1% across the surface of a 2" diameter wafer sample located at the centeral plane of the coils.

b. Sample mounting system

The current sample mounting system shown in Figure 7 was designed for use with 1" diameter wafers. This unit, constructed from teflon, has a 1" diameter recess in which the sample is firmly held. With this holder mounted on a precision X-Y translation stage, it is possible to achieve accurate and repeatable sample positioning. Furthermore, the X-Y translation stage allows homogeniety studies to be done on any wafer if desired. Design drawings are included in Appendix I .

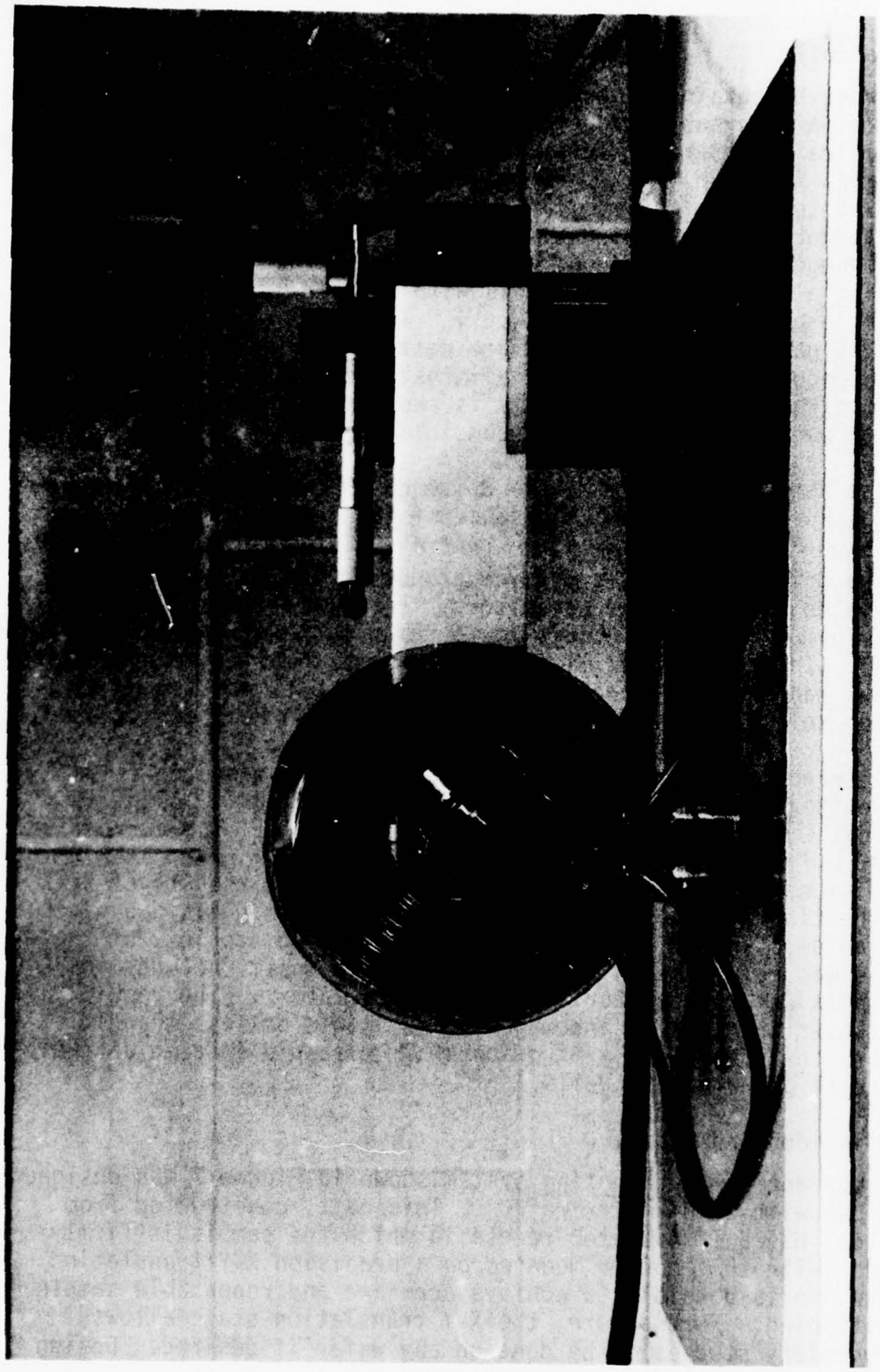

Figure 6. Photo of drive coils.

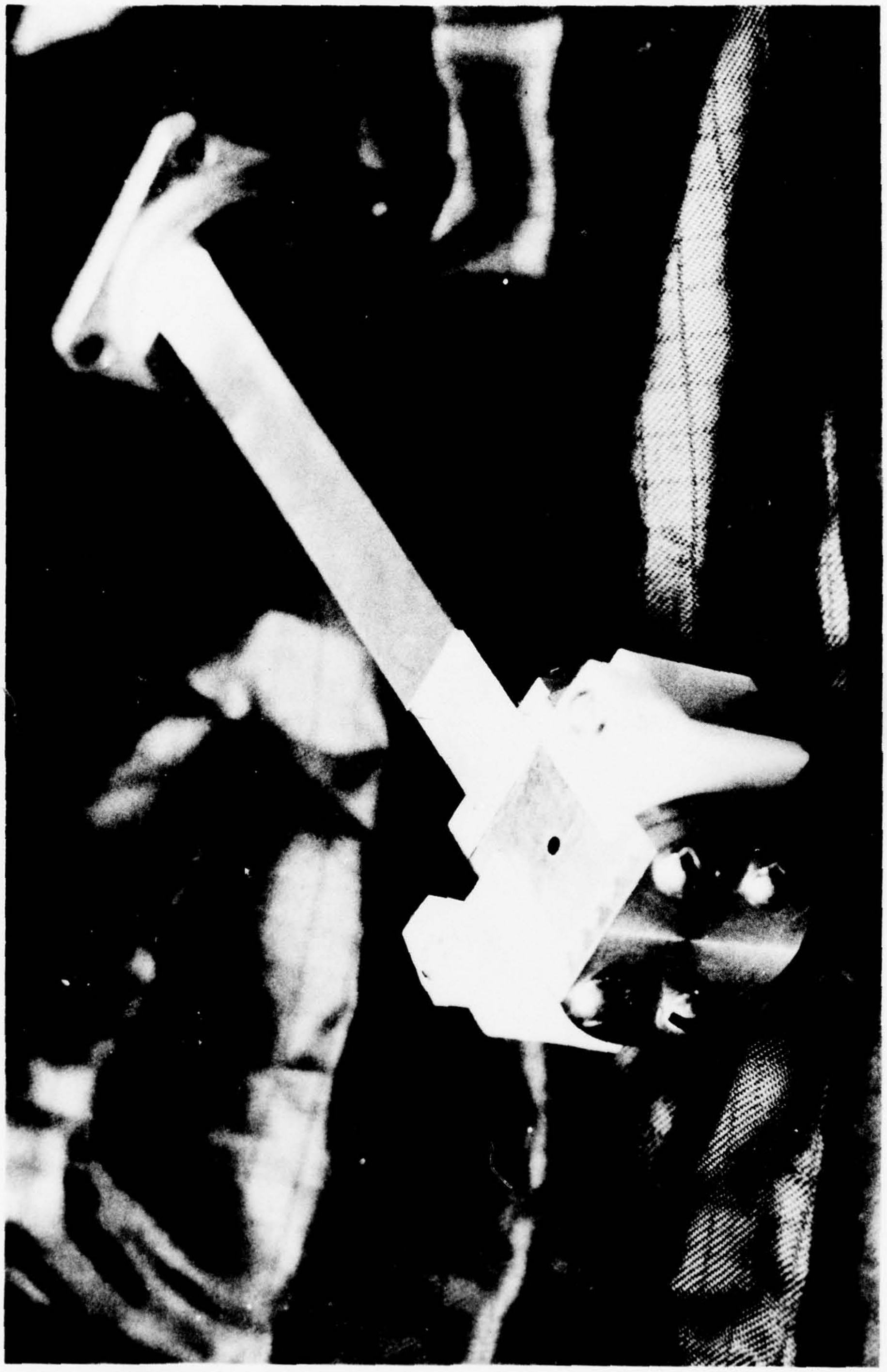

Figure 7. Photo of sample mounting system.

TABLE 1

DRIVE COILS: DC CHARACTERISTICS

I (Amps)	H (oe.)
1	26.1
2	51.3
5	123
8	196
10	243
12	291
14	338
16	386
18	434
20	484

System Resistance (Coils in Parallel)

$R = .7\Omega$

TABLE 2

DRIVE COILS: AC CHARACTERISTICS (LEXAN)

f(Hz)	C(μf)	I(AMPS)	R_{sense}	V_{sence}	V_{power}	R_{eff}
213	100	52	.05	2.6	10	.54
238	80	52	.05	2.6	10	.54
273	60	51	.05	2.55	10	.55
299	50	51	.05	2.55	10	.55
312	45	51	.05	2.55	10	.55
475	18	56	.025	1.4	15	.66
650	11	56	.025	1.4	15	.75
900	5	35	.05	1.7	10	.8

I = Current through coil system (Peak-Peak)

V = Power Supply Voltage (RMS)

V_{sence} = Voltage Across Sense Resister Network (Peak-Peak)

$$R_{eff} \equiv V_{power} \Big/ \frac{I}{2\sqrt{2}}$$

c. Pickup coils

The pickup coils are each wound with 100 turns of # 34 gauge copper wire on delrin forms shown in Appendix II. The sample pickup coil is located on the Helmboltz coil axis and approximately 2 mm from the sample. For this coil to sample separation, it is estimated that the induced voltage signal due to the sample will be on the order of .2mV. Further details are given in Appendix I. The voltage signal due to the changing drive field is known to be on the order of 20 mV. Thus a second "compensation" pickup coil is required positioned as shown in Figure 5. This coil will provide a signal to null out the unwanted 20 mV signal due to the changing drive field H_D. To date it has been possible to null out this signal to less than .2 mV P-P, however, this is not sufficient as the expected signal due to changes in the sample magnetization is of the same order of magnitude. It is probable that by improving the rigidity of the drive coils and pickup coil mount supports the background signal null can be improved greatly. Work towards this goal is currently underway and should be completed in the near future.

d. System electronics

In order to null out the backround signal due to $H_D(+)$ a multiarm compensation bridge has been constructed. This bridge, originally designed by Huber[6] for use in M-H loopers, has several branches which can be adjusted to null out the fundamental and higher order harmonic signals from the pickup coils. This bridge circuit along with the amplifying and integrating circuit is shown in Figure 8.

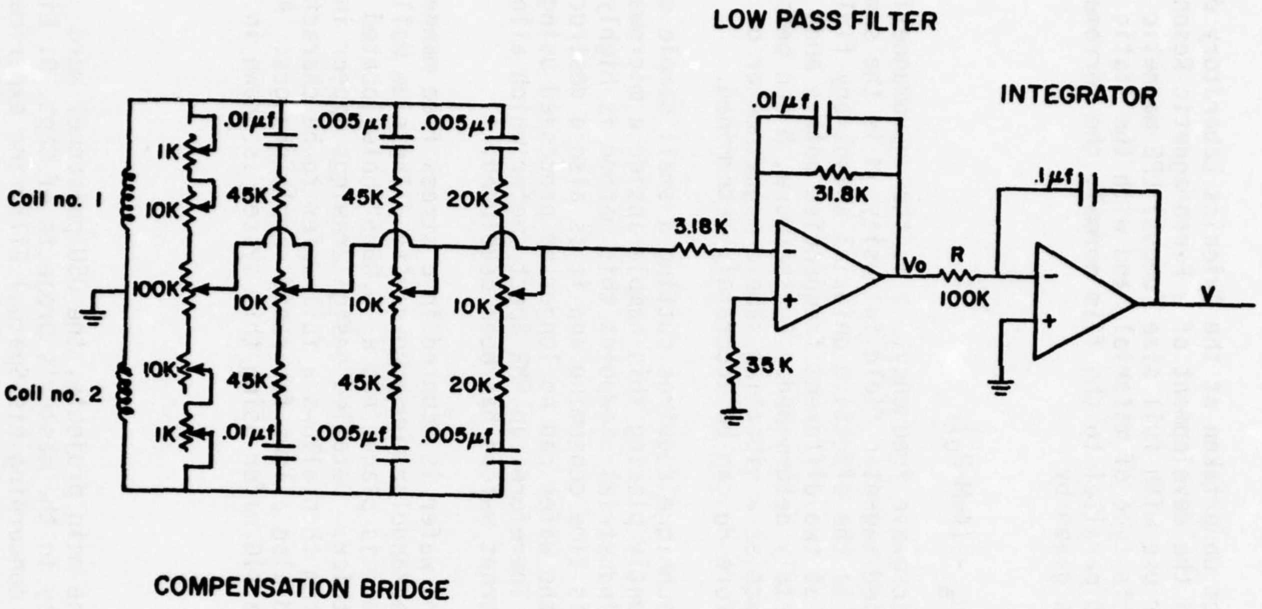

Figure 8. Circuit diagram for M-H looper electronics.

2. Ferromagnetic Resonance

The second project undertaken at the Avionics Laboratory during the last year has been the development of a Ferromagnetic Resonance (FMR) Spectrometer for use with full size (uncut) LPE magnetic bubble garnet wafers. For this type of material and with the static magnetic field applied parallel to the film normal, the ferromagnetic resonance condition is given by

$$\frac{\omega}{\gamma} = H_a - (4\pi M - H_u).$$

Here ω is the radial microwave frequency, γ is the gyromagnetic ratio, H_a is the applied magnetic field intensity, M is the sample magnetization, and H_u is the effective uniaxial anisotropy field. If measurements are made at two different frequencies both γ and $(4\pi M - H_u)$ can be accurately determined. Furthermore, M can be measured by other techniques such as a vibrating sample magnetometer or an M-H looper, and therefore H_u can be accurately determined.

The normal FMR technique requires cutting a small sample out of the wafer and subsequently placing this sample inside a microwave cavity. From an industrial viewpoint this method is highly undesirable since it is time consuming and it is also a destructive testing technique as the wafer can no longer be processed using automated equipment. Therefore, an FMR Spectrometer which allows the use of full LPE garnet wafers has been developed.

In this system the wafer is mounted in a stress free manner on the outside of a rectangular microwave cavity. The side wall against which the sample is placed has a 0.0625" hole located in the center and is 0.010" thick. Detailed design drawings appear in Appendix I . This system then allows a full wafer to be characterized without the damage and also allows for rapid sample changes. A typical spectra from a YIG wafer using this system is shown in Figure 9.

Misc.

In addition to the main projects, the OSU personnel were involved in a minor way in the master's projects of Capt. R. Eiles and Capt. R. McDonald concerning his Spatual Filtering experiment. Also microscope coils were designed for Eiles bubble mobility experiment.

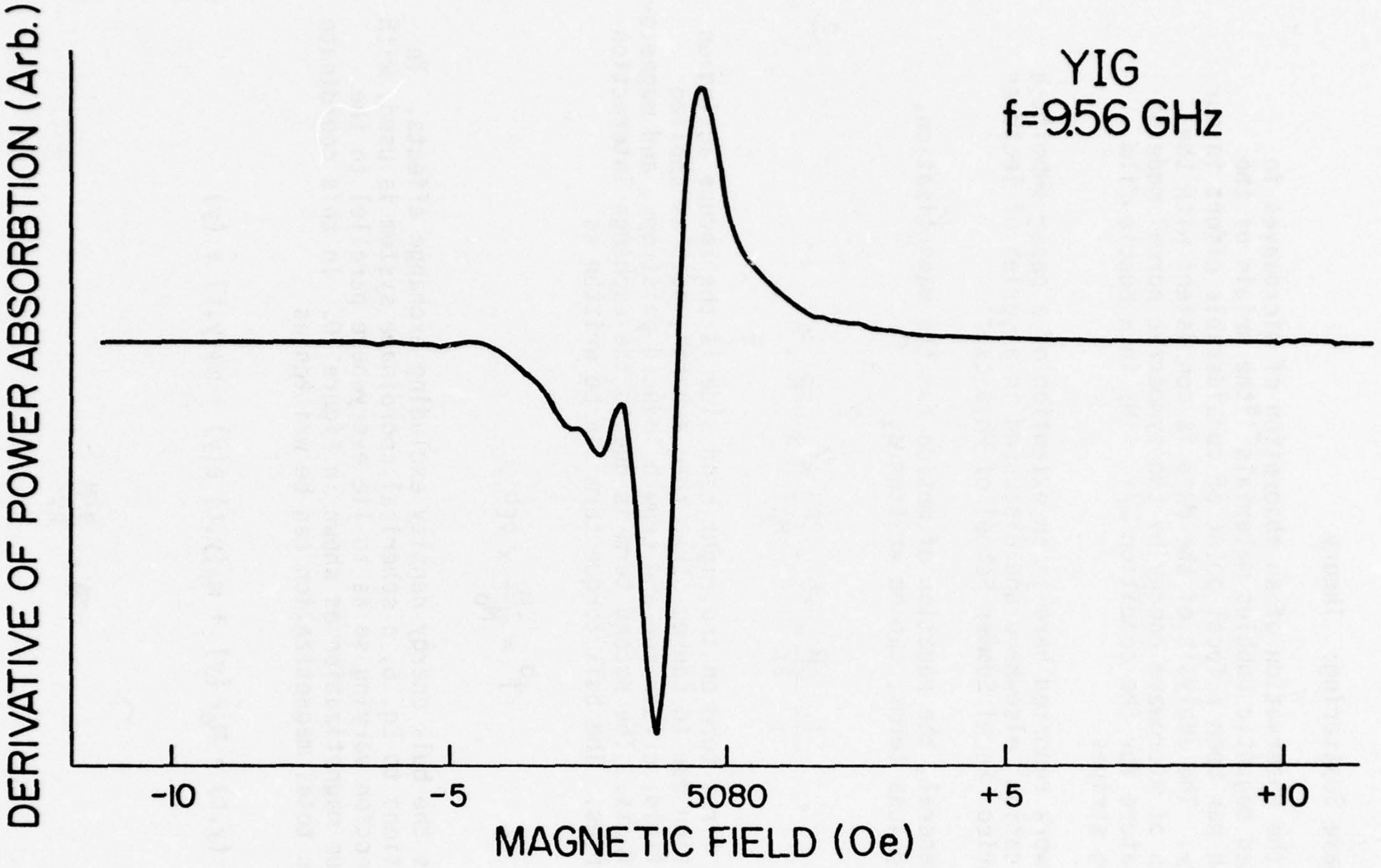

Figure 9. Ferromagnetic resonance spectra from a full wafer YIG sample at 9.56 GHz and the magnetic field applied normal to the film plane.

1. Spinwave Scattering: Theory

With the observation of an absorption of microwaves in unsaturated magnetic bubbles materials[7,8] the origin of the absorption has been a focal point of considerable effort in our laboratory. The analysis of the data is consistent with the absorption of microwave energy by the symmetric normal mode of unbound nature for the condition $\omega/\gamma > H_k$ in a bubble film containing stripes.

The work reported here is an extention of a paper submitted for publication[9] elsewhere and discussed in a series of lectures at the Enrico Fermi Summer School of Physics.[10]

In general, the equation of motion for the magnetization, neglecting loss terms, can be written as

$$\frac{1}{\gamma}\frac{\partial \vec{M}}{\partial t} = \vec{T}^b + \frac{2A}{M_o^2}\vec{M} \times \nabla^2\vec{M} \,, \qquad (6)$$

where the first term on the right hand side is the torque acting on magnetization due to causes other than exhanqe, such as applied magnetic field, crystaline and growth induced anistropy, and magnetostatic effects. The second term is due to the exchange interaction between spins. The bulk torque term can be written as

$$\vec{T}^b = \frac{-M}{M_o} \times \nabla E^b \,. \qquad (7)$$

Here E^b is the bulk energy density excluding exchange effects. To find solutions to Eq. 6, a spherical coordinate system is used, with the $\hat{r}$ direction varying so as to lie everywhere parallel to the equilibrium magnetization as shown in Figure 10. In this coordinate system the total magnetization can be written as

$$\vec{M}(y,t) = M_o\hat{r}(y) + m_\theta(y,t)\,\hat{\theta}(y) + m\phi(y,t)\,\hat{\phi}(y) \qquad (8)$$

and

$$\nabla^2\vec{M} = \frac{\partial^2 M}{\partial y^2} \qquad (9)$$

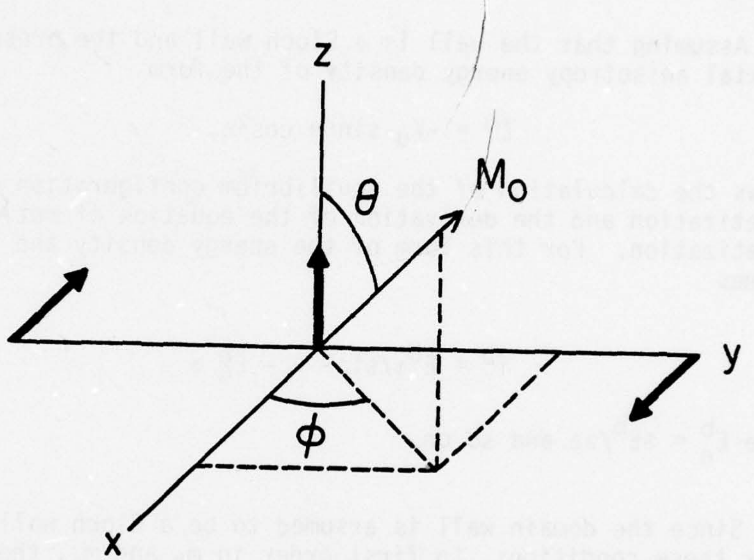

Figure 10. Coordinate system used in derivation of equation of motion for a spin wave in a domain wall.

Using standard mathematical techniques, the derivitives of the unit vectors are

$$\hat{r}' = \theta'\hat{\theta} + \phi'\sin\theta\hat{\phi}$$

$$\hat{\theta}' = -\theta'\hat{r} + \phi'\cos\theta\ \hat{\phi} \qquad (10)$$

$$\hat{\phi}' = \phi'\sin\theta\hat{r} - \phi'\cos\theta\hat{\theta}$$

where primes denote differentiation with respect to y.

Assuming that the wall is a Bloch wall and the presence of a uniaxial anisotropy energy density of the form

$$E^b = -K_u \sin^2\theta \cos^2\phi, \qquad (11)$$

allows the calculation of the equilibrium configuration of the magnetization and the derivation of the equation of motion of the magnetization. For this form of the energy density the torque becomes

$$\vec{T}^b = E^b{}_\phi/\sin^\theta\ \hat{\theta} - E^b_\theta\ \hat{\phi} \qquad (12)$$

where $E^b_\theta = \partial E^b/\partial\phi$ and so on.

Since the domain wall is assumed to be a Bloch wall, $\phi=\phi'=\phi''=0$. Under these conditions, to first order in m_θ and m_ϕ, the transverse components of the magnetization are

$$\vec{M} \times \nabla^2\vec{M} = (M_o m_\phi \theta'')\hat{r} + (-M_o m(\theta')^2 - M_o m\phi')\hat{\theta} + (-M_o m_\theta(\theta')^2 + M_o^2\theta'' + M_o m_\phi'' + M_\theta(\theta')^2)\hat{\theta} \qquad (13)$$

To find the equilibrium condition, only terms to zeroth order in m_θ and m_ϕ need to be considered, and Eq. 13 reduces to

$$\vec{M} \times \nabla^2 M = M_o^2\ \theta''\hat{\phi}. \qquad (14)$$

For the static case, the equation of motion becomes

$$-\vec{T}^b = \frac{2A}{M_o{}^2}\vec{M} \times \nabla^2\vec{M}\ . \qquad (14)$$

The θ component of this equation is identically equal to zero and the ϕ component becomes

$$-2K_u \sin\theta \cos\theta = 2A\theta''. \tag{16}$$

The solution to this equation is the Gudermannian function

$$\theta(\eta) = \mathrm{gd}\,(\eta) = 2\tan^{-1}(e^{\eta}) - \pi/2, \tag{17}$$

where $\eta = (\frac{K_u}{A})^{1/2}$ and is shown in Figure 11.

Due to small deviations of the magnetization from its equilibrium configuration, additional terms must be included in the torque. These terms will be of the form

$$\delta\vec{T}^b = -\frac{\delta\vec{M}}{M_o} \times \delta\nabla E^b. \tag{18}$$

The first term is

$$\frac{-\delta\vec{M}}{M_o} \times \nabla E^b = \frac{-1}{M_o}(m_\theta E^b_\phi \csc\theta - m_\phi E^b_\theta)\hat{r}. \tag{19}$$

Since $M_o\delta\theta = m_\theta$ and $M_o\delta = m_\phi/\sin\theta$ the second term is

$$\frac{-\vec{M}_o}{M_1} \times \delta\nabla E^b = \frac{1}{M_o}\left[\left\{ m_\phi(E^b_\theta \cot\theta + E^b_{\phi\phi} \csc^2\theta) + m_\theta(E^b_{\theta\phi}\csc\theta - E^b_\phi\cot\theta\csc\theta\right\}\right]\hat{\theta} \tag{20}$$
$$- \left\{ m_\theta E^b_{\theta\theta} + m_\phi(E^b_{\theta\phi}\csc\theta - E^b_\phi \cot\theta)\right\}\hat{\phi}$$

Making use of these additional terms and of the equilibrium condition of Eq. 16 to first order in m_θ and m_ϕ, the equation of motion becomes

$$\frac{1}{\gamma}\frac{\partial m\theta}{\partial t} = E^b_\phi \csc\theta + \frac{1}{M_o}\left[m_\phi(E^b_\theta \cot\theta + E^b_{\phi\phi} \csc^2\theta) + m_\theta(E^b_\phi \csc\theta\cot\theta\right]$$
$$\frac{-2A}{M_o}((\theta')^2 m\phi + m_\phi'') \tag{21}$$

$$\frac{1}{\gamma}\frac{\partial m\phi}{\partial t} = \frac{1}{M_o}\left[-m_\theta E^b_{\theta\theta} + m_\phi (E^b_\phi \cot\theta \csc\theta - E^b_{\theta\phi}\csc\theta\right] + \frac{2A}{M_o} m_\theta''$$

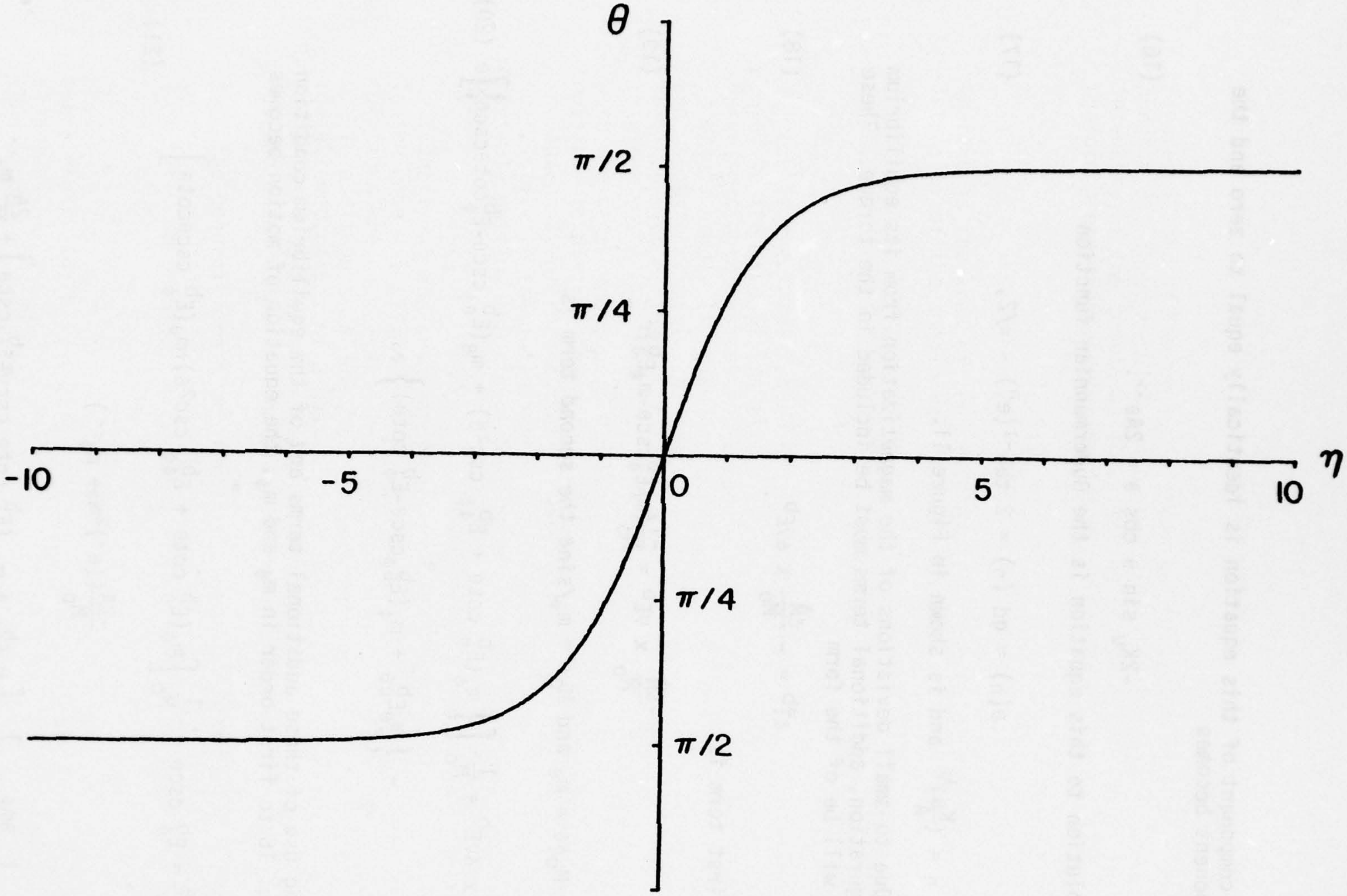

Figure 11. θ vs. η for equilibrium condition.

For a uniaxial anisotropv energy density for the form given in Eq.11, the derivitive terms are

$$
\begin{aligned}
E^b_\theta &= 2K_u \sin\theta \cos\theta, \\
E^b_\phi &= 0, \\
E^b_{\theta\phi} &= 0, \\
E^b_{\theta\theta} &= -2K_u \cos 2\theta \quad . \\
E^b_{\phi\phi} &= 2K_u \sin^2\theta
\end{aligned}
\tag{22}
$$

Substituting these into Eq. 21, converting to the dimensionless variable η and using the fact that $\theta = \frac{d}{d\eta} gd(\eta) = \operatorname{sech} \eta$ gives

$$\frac{1}{\gamma} \frac{\partial m_\theta}{\partial t} = \frac{2K_u}{M_o} (1-\cos^2\theta-\operatorname{sech}^2\eta)\, m_\phi - \ddot{m}_\phi$$

and (23)

$$\frac{1}{\gamma} \frac{\partial m_\phi}{\partial t} = \frac{2K_u}{M_o} \left[\cos 2\theta m_\theta + \ddot{m}_\phi\right]$$

where dots denote differentiation with respect to η. Assuming a time dependence of the form $e^{i\omega t}$ these equations reduce to the form

$$
\begin{aligned}
m_\theta &= \frac{-i}{\Omega} \left[(1-\cos^2\theta - \operatorname{sech}^2\eta) m_\phi - \ddot{m}_\phi\right] \\
m_\phi &= \frac{+i}{\Omega} \left[\cos 2\theta\, m_\theta + \ddot{m}_\theta\right]
\end{aligned}
\tag{24}
$$

wherc $\Omega = \frac{\omega M_o}{2\gamma K_u}$. These equations can de decoupled by differentiating the second and substituting it into the first, giving

$$\ddot{\ddot{m}}_\theta = a(\eta,\theta)\, m_\theta + b(\eta,\theta)\, \dot{m}_\theta + c(\eta,\theta) \ddot{m}_\theta \tag{25}$$

where

$$
\begin{aligned}
a(\eta,\theta) &= \sin^2\theta\cos 2\theta + 3\cos 2\theta\,\mathrm{sech}^2\eta + \sin^2 2\theta + \Omega^2 \\
b(\eta,\theta) &= 4\sin 2\theta\,\mathrm{sech}\,\eta \\
c(\eta,\theta) &= \sin^2\theta - \mathrm{sech}^2\eta - \cos 2\theta
\end{aligned}
\tag{26}
$$

The functional form of these coefficients is shown in Figure 12 For large values of η, the coefficients become constants and solution of of the form $e^{k\eta}$ can be assumed. In this case, the allowed values for the wave vector k are

$$
\begin{aligned}
K^2_{1,2} &= 1+\Omega \\
K^2_{3,4} &= 1-\Omega
\end{aligned}
\tag{27}
$$

There are two distinct types of solution for m_θ, depending on the value of Ω. For the case $\Omega > 1$, k_3 and k_4 are imaginary, giving rise to ocillitory components in m_θ. In this case the k_1 and k_2 terms do not contribute since one is negligible for large values of η and the other is unbounded and therefore unphysical. For the case $\Omega<1$, all four foots are real; two of the terms are very small and two unbounded and therefore cannot contribute to the solution. The solution for the transverse magnetization is a solution which is nonzero only near the center of the wall.

There are then two types of solution to Eq. 25 in different regions of the excitation frequency. For $\Omega>1$, the domain wall would act as a source of traveling spinwaves. For $\Omega<1$, the solution would be a spinwave mode localized in the domain wall and decaying to zero amplitude outside the wall, a bound spinwave exitation.

In the case $\Omega>1$, Eq. 25 can be solved numerically, provided the values of m_θ and its derivitives are known at some initial point. Since only solutions which have a net magnetic dipole moment are experimentally observable, any solution of interest will be symetric about the center of the wall. A Runge-Kutta method was used to obtain solutions for the transverse magnetization for a variety of frequencies, starting at the center of the wall and working outwards. The symmetry condition requires that the first and third derivitives of m_θ be equal to zero at $\eta = 0$. The value of m_θ at the origin can be arbitrary, since it determines the amplitude of the spinwave. In this work, the value of the second derivitive of m_θ at the origin was found by trial and error, varying $\ddot{m}_\theta(0)$ until oscilations of equal positive and negative amplitude were found in regions far from the center of the wall. The results of these calculations are shown in

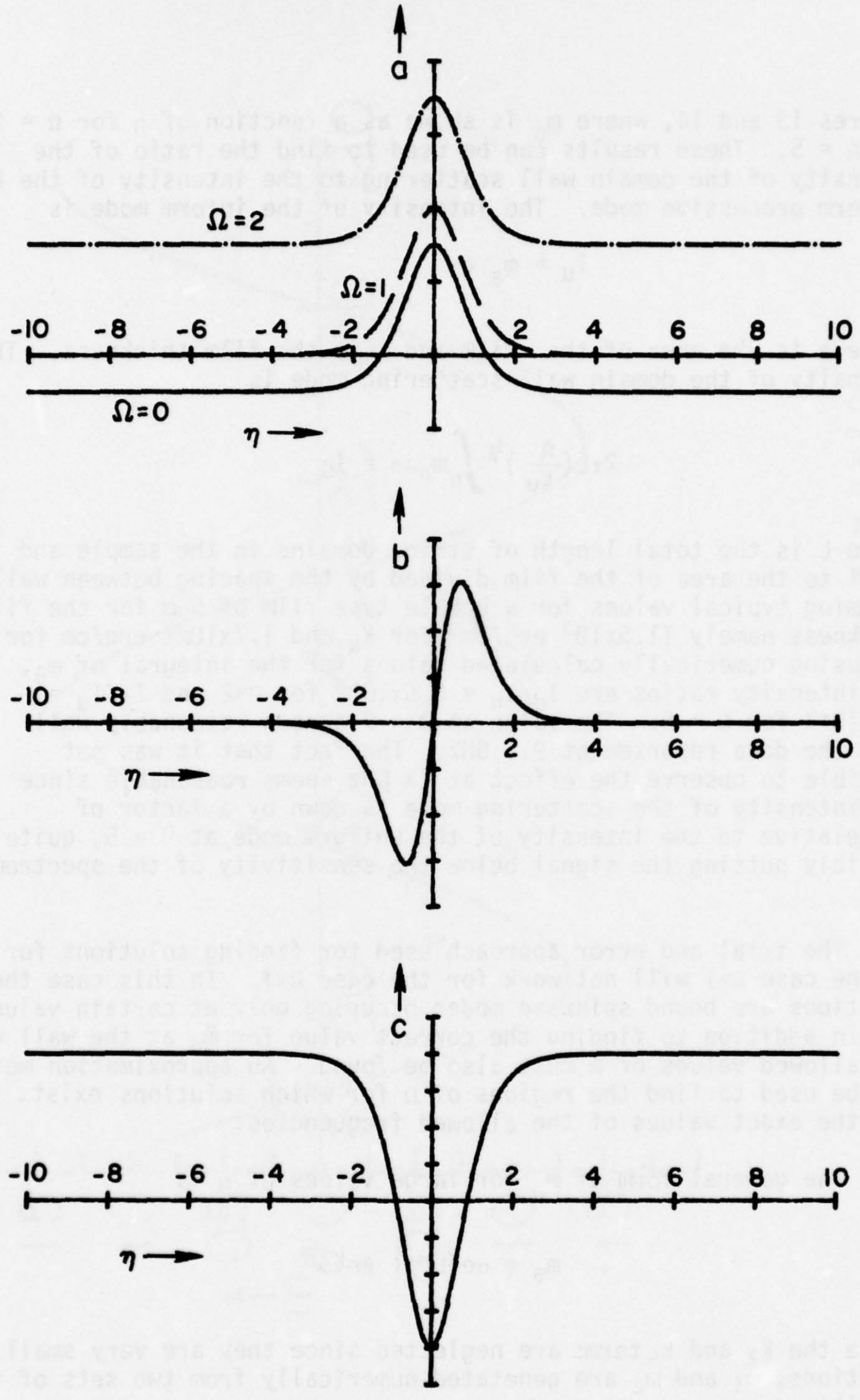

Figure 12. Coefficients of eq. 25, given in eq. 26.

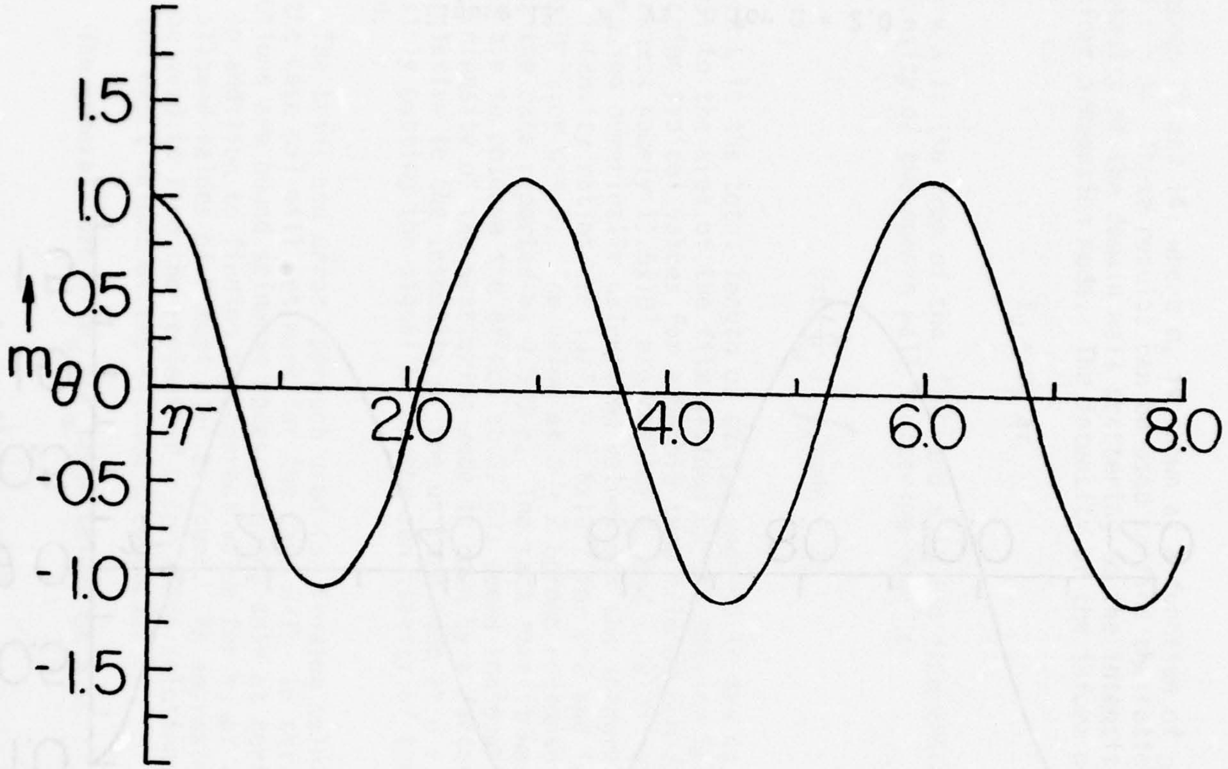

Figure 14. m_θ vs. η for $\Omega = 5.0$

$$m_1(0)=1; \quad \ddot{m}_1(0)=0$$
$$m_2(0)=0; \quad \ddot{m}_2(0)-1 \tag{31}$$

By using the known assymptotic values of k_1 and k_3, using the values of m_1 and m_2 at two different values of η, the values of the coefficients α and β which generate the solutions m_1 and m_2 can be calculated. The *bounded solution* m_θ *is then a linear combination of the two unbounded* solutions

$$m_\theta = m_1 + xm_2 \tag{32}$$

Requiring m_θ to be zero for large values of η is equivalent to requiring

$$\alpha_1 + x\alpha_2 = 0$$
$$\beta_1 + x\beta_2 = 0 \tag{33}$$

Rearranging, this requirement becomes

$$x = \alpha_1/\alpha_2$$
$$P = \alpha_1\beta_2 - \alpha_2\beta_1 = 0 \tag{34}$$

Thus, the allowed values of Ω can be approximated by calculating P as a function of Ω and finding the regions where g crosses zero. The result of this calculation, as presented in Figure 15, show that in this approximation, no bound states are predicted.

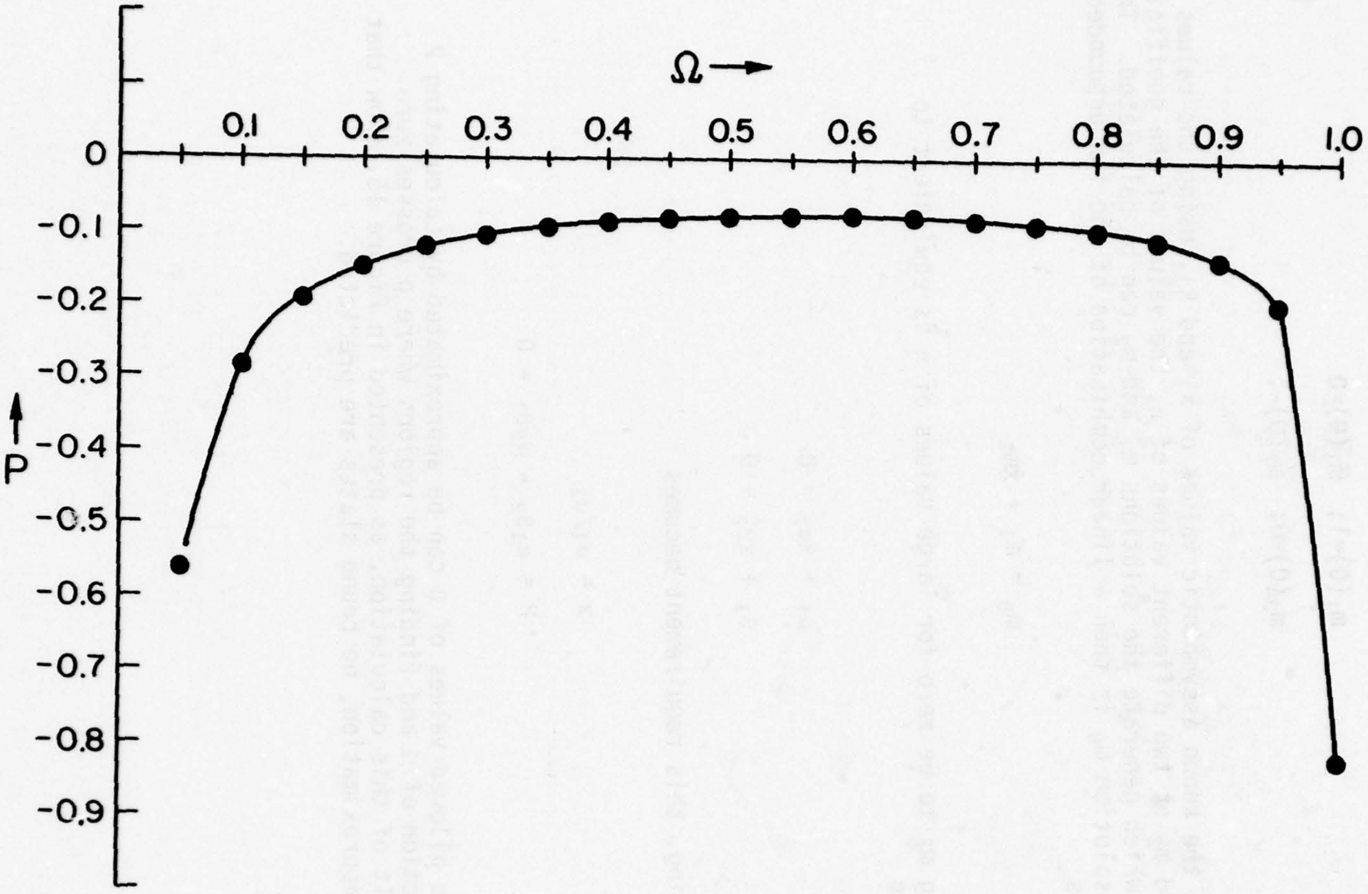

Figure 15. P vs. Ω, predicting the existence of no bound states.

2. Spinwave Scattering: Experiment

The use of magnetic resonance for measurement of the bubble collapse field, H_{col}, and bubble stripout field, H_{so}, has been reported[7] [8].

During a systematic investigation of the ferromagnetic resonance absorption characteristics of magnetic bubble materials, a low-field change in microwave susceptibility was observed as shown in Figure 16. The shift was found to be repeatable but to depend on whether the magnetic field was decreasing or increasing. The shifts in the susceptibility were found to be correlated with the bubble collapse field or stripe collapse field for increasing field sweep and the bubble strip-out field for decreasing field sweep.

A standard X-band microwave spectrometer operating at 9.52 GHz was used for these measurements. The high-field ferromagnetic resonance spectrum was observed from (111) oriented films in one of two conditions. The internal field, H_{int}, determined when the magnetization is normal to the film surface (out-of-plane resonance) is composed of the induced anistropy field, H_u, the cubic anistropy field, H_K, and the demagnetization field, $H_d = -4\pi Ms$, i.e. $H_{int} = H_u + 2/3H_K - 4\pi Ms$. If ω/γ, where γ is the gyromagnetic ratio, is greater than H_{int}, one line was observed in the out-of-plane resonance orientation and another was observed for the in-plane resonance orientation. In those films for which ω/γ was less than H_{int}, an out-of-plane resonance was not observed while two modes were observed in the in-plane resonance orientation.

In addition to the high field ferromagnetic resonance lines, a change in microwave susceptibility was also observed at low fields for the magnetic field in the out-of-plane orientation. Operating the spectrometer in the derivative presentation mode, this change in microwave susceptibility appeared as a peak with a distinctive nonresonance shape for up-field and down-field sweeps. The intensity of these signals is two to three orders of magnitude weaker than the high-field ferromagnetic resonance signals. Figure 16 is the spectra obtained for a sample having stripe domains as the initial state at zero field. The presence of the peak at the high field end of the sweep is very dependent on the magnetic field modulation amplitude. The position of the high field cut-off is observed to increase with increased modulation amplitude and at large amplitude modulation it also tends to wash out the characteristic differences in the stripe collapse and stripout field values.

Figure 17 is the spectra obtained for a sample having a bubble lattice as the initial state at zero field with the bubble diameter decreasing with increasing field. This condition was created by applying a large (5000 Oe) field in the plane of the film and reducing it to zero. In bubble samples, the enhanced peak characteristic of stripe collapse is not present and the disappearance of the absorption is observed to occur at higher fields. As the magnetic field is reduced, the characteristic signal associated with stripe formation is observed.

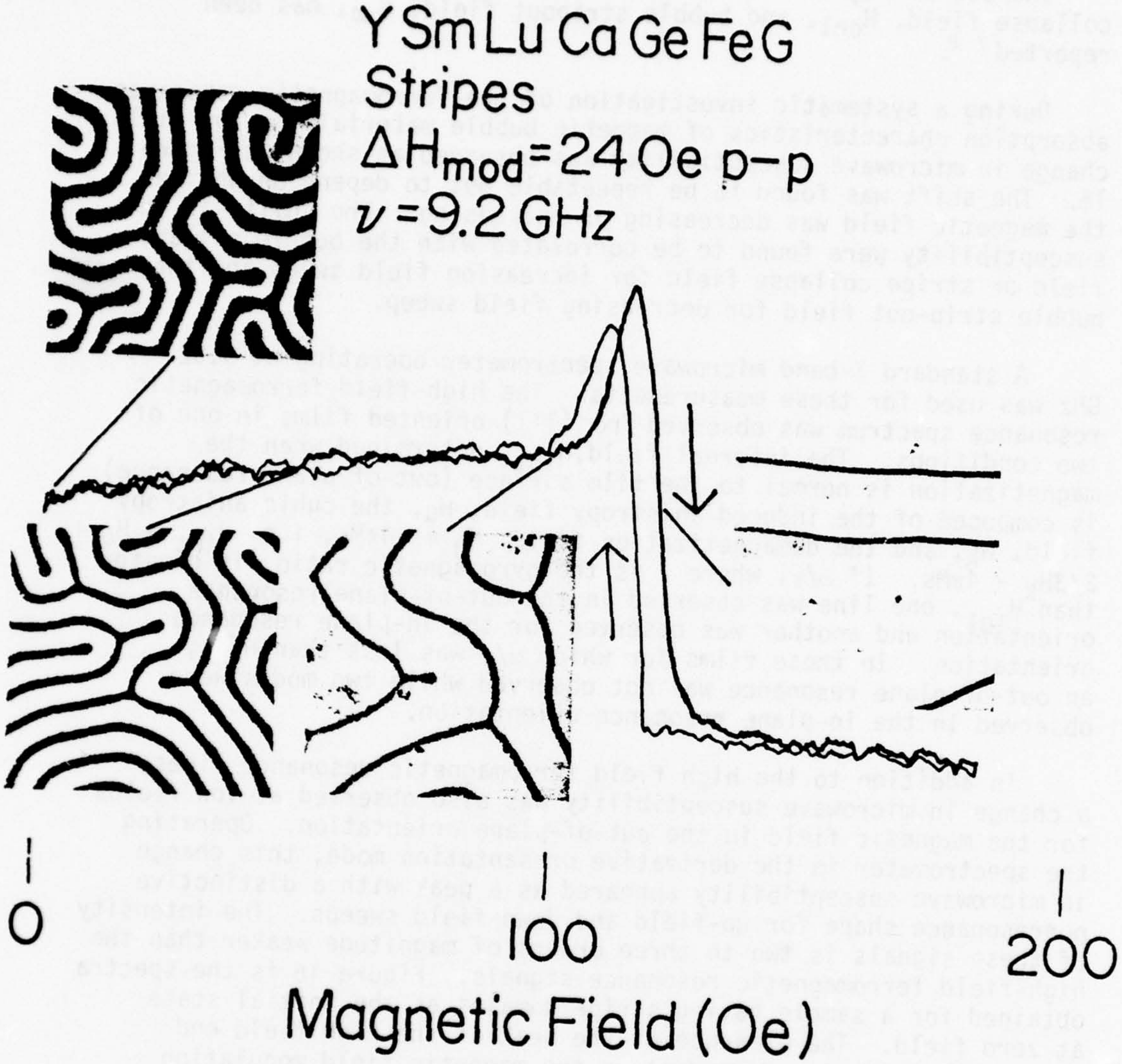

Figure 16. The microwave signal observed in a magnetic bubble material when the starting configuration is that of stripes in the sample. The absorption is strongly dependent on the modulation amplitude.

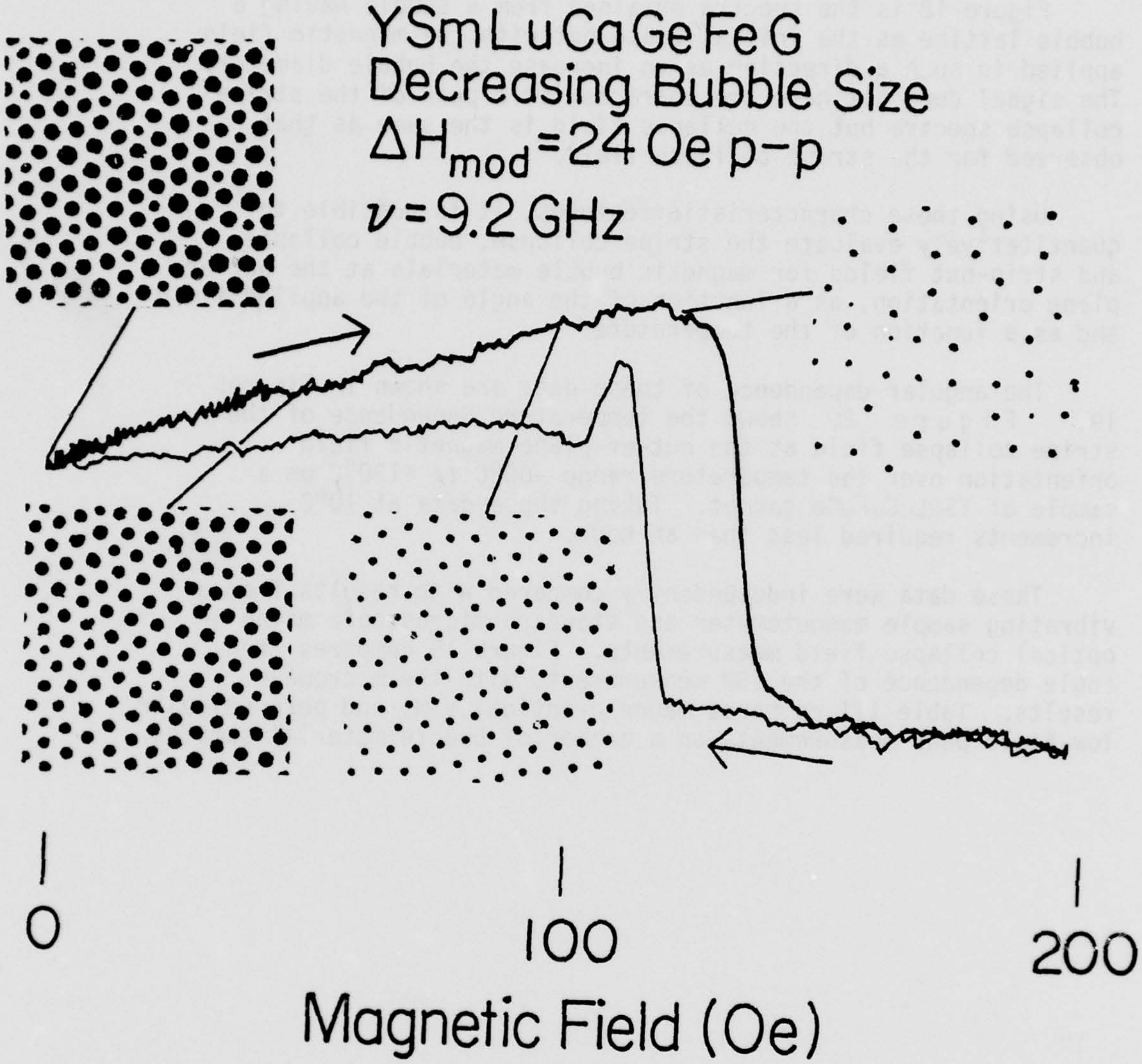

Figure 17. The microwave signal observed in a magnetic bubble material when the starting magnetic configuration is a bubble lattice. The bubbles are decreasing in size with increasing field. As the magnetic field is returned to zero field, the stripe configuration is created in the film.

Figure 18 is the spectra obtained from a sample having a bubble lattice as the initial state but with the magnetic field applied in such a direction as to increase the bubble diameter. The signal does not have the characteristic peak of the stripe collapse spectra but the collapse field is the same as that observed for the stripe collapse field.

Using these characteristic features, it is possible to quantitatively evaluate the stripe collapse, bubble collapse and strip-out fields for magnetic bubble materials at the out-of-plane orientation, as a function of the angle of the applied field and as a function of the temperature.

The angular dependence of these data are shown in Figures 19. Figure 20 shows the temperature dependence of the stripe collapse field at the out-of-plane magnetic field orientation over the temperature range -60^0C to $+130^0$C on a sample of YSmLuCaFeGe garnet. Taking these data at 10^0C increments required less than an hour.

These data were independently compared with results from a vibrating sample magnetometer and standard microscopic magneto-optical collapse field measurements. Figure 19 compares the angle dependence of the VSM measurements with the microwave results. Table III compares magneto-optical,VSM, and perpendicualr low-field peak measurements on a number of bubble material samples.

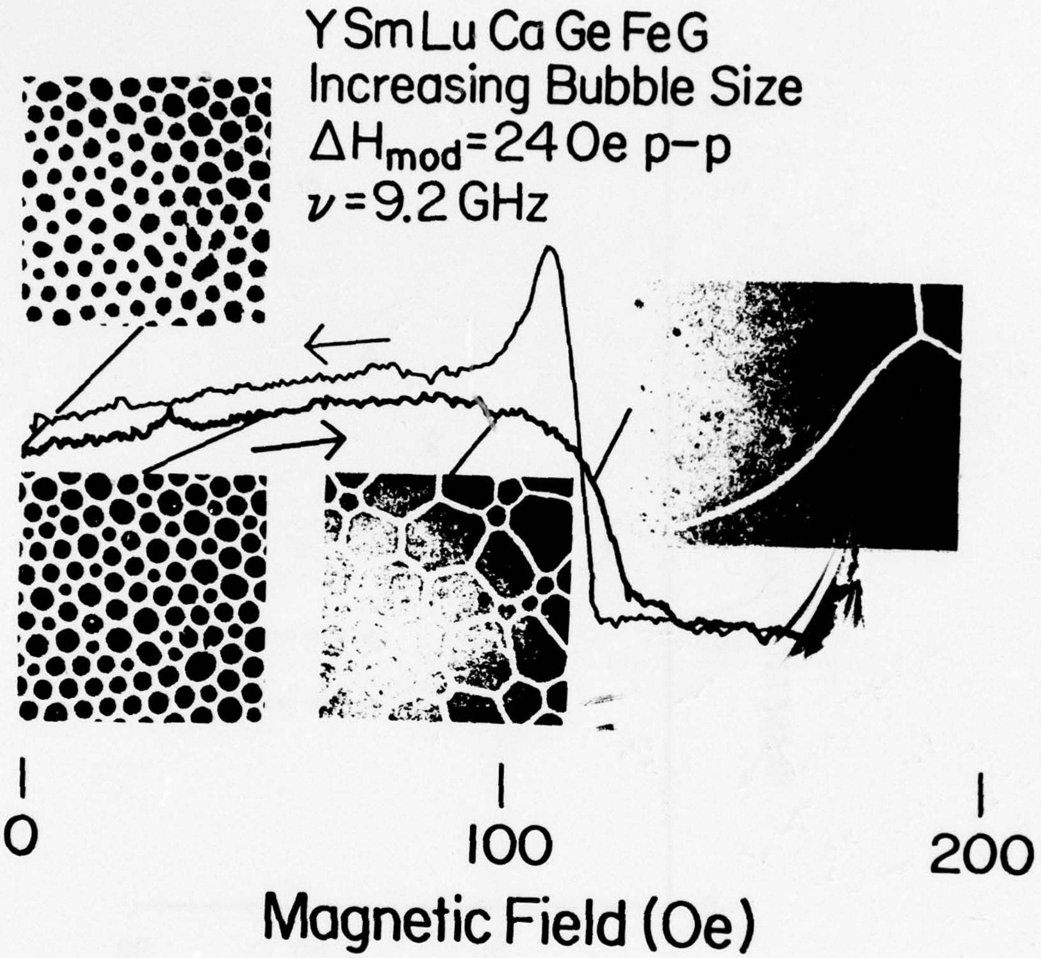

Figure 18. Microwave signal in a magnetic bubble material whose initial configuration is bubble domains. Bubble size increases with increasing applied H.

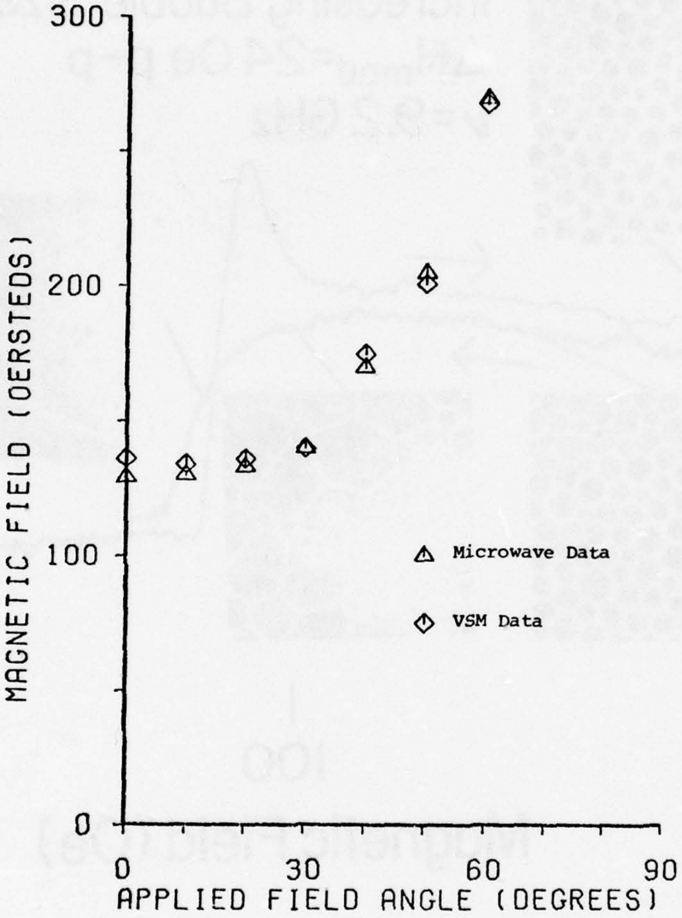

Figure 19. Angle dependence of the collapse field as observed by vibrating sampel magnetometer (VSM)and by low field microwave susceptibility changes.

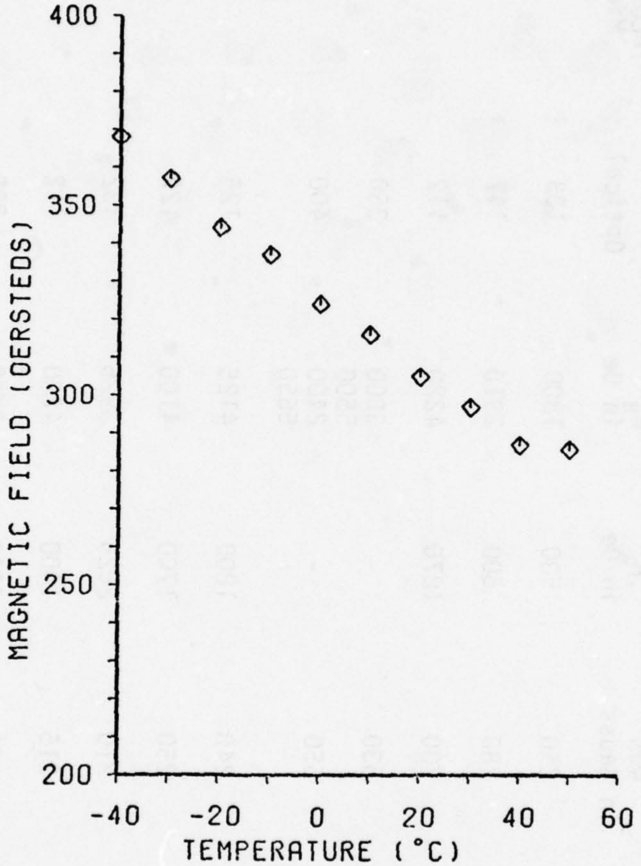

Figure 20. The stripe collapse field observed in the out of plane magnetic field orientation over the temperature range indicated on a sample of YSmLuCaGeFe garnet.

TABLE 3

BUBBLE FILM CHARACTERISTICS AND MICROWAVE COLLAPSE FIELD MEASUREMENTS.

Film	Components	$4\pi M$ in Gauss	$H_\perp$ in Oe	$H_\parallel$ in Oe	H_{coll} in Oe		
					Optical	Microwave	VSM
5421	YEuCaSiGeFe	250	500	1800	133	150	-
5444	YEuCaSiGeFe	280	600	2910	147	170	-
5696	YSm Ca Fe	200	1870	4220	112	98	112
H62	YSm Lu Ga Fe	530	-	3000 5500	350	310	310
H99	YSm Lu Ga Fe	650	-	2400 5650	400	420	440
5692	YSmLuCaGeFe	240	1800	4125	125	110	134
5702	YSmLuCaGeFe	250	1700	4100	122	115	
5804	YSmLuCaGeFe	210	2025	3925	132	115	125
330	YSmLuCaGeFe	215	1400	4200	112	100	110
Y209	YSmLuCaGeFe	400	2500	3700	225	180	185
Y229	YSmLuCaGeFe	330	2400	3800	175	-	195

3. Radio Frequency Effects in Bubble Materials

In addition to the microwave absorption experiment, absorption was also observed at radio frequencies near 15 MHz as shown in Fig. 21. These signals are observed to have very complex frequency and angular dependences which are not well understood at this time.

To study these effects in more detail, a RF spectrometer was developed over the past year.

The RF spectrometer is diagramed in Fig. 22. The heart of this system is the hybrid magic tee. This four port device operates as follows: whenever the impedance of the two side arms (C & D) are matched, the opposite arms (A & D) are isolated from each other. In theory this isolation is complete, but in practical devices this ideal limit is not attained; the maximum isolation in the hybrids used is 35-40 dB. If the impedance at the two side arms are not matched, the isolation decreases with the degree of mismatch until there is only a very small insertion loss (typically 1 dB)is present. In actual operation, the system is adjusted so that there is no power absorption by the sample and the impedance matching network of the sample probe is then adjusted to precisly match the impedance of the probe to the 50Ω dummy load on the other side arm. Then, if the impedance of the probe should change by an amount δZ, an additional voltage $\delta V = \frac{1}{2}\delta Z\ v_0/R_0$ will appear at the output port of the magic tee. Here R_0 is the characteristic impedance of the system and V_0 is the voltage at the input port of the hybrid.[11]

A variety of sample probes are useable with this system. At relatively low frequencies, a coil can be used to couple the RF field to the sample. At higher frequencies, the parasitic capacitance of the coil limits its utility and a R-F cavity must be used. If an untuned system is desired, a suitably constructed helical transmission line can be used to couple to the sample.

Up to this point in time, only coils have been used. The equivilent circuit for a coil type probe is shown in Fig. 23. C_s is the shunt capacitance present in the system, consisting of the capacitance of the coil itself and the capacitance of the cable connecting the coil to the matching network. C_1 primarily adjusts the resonance frequency of the coil and C_2 adjusts the impedance looking into the network. These capacitors are low loss ceramic trimmer capacitors in parallel with silver mica fixed capacitors. They are mounted rigidly in a box milled out of a solid block of aluminum to minimize microphonics. The box is mounted at the end of a rigid low capacitance coaxial cable with locking coaxial connectors. The cable, constructed from copper pipe with an I.D. of 7/8" and a center conductor of 1/16" brass rod centered with nylon spacers, has a capacitance of 9.5 pF.

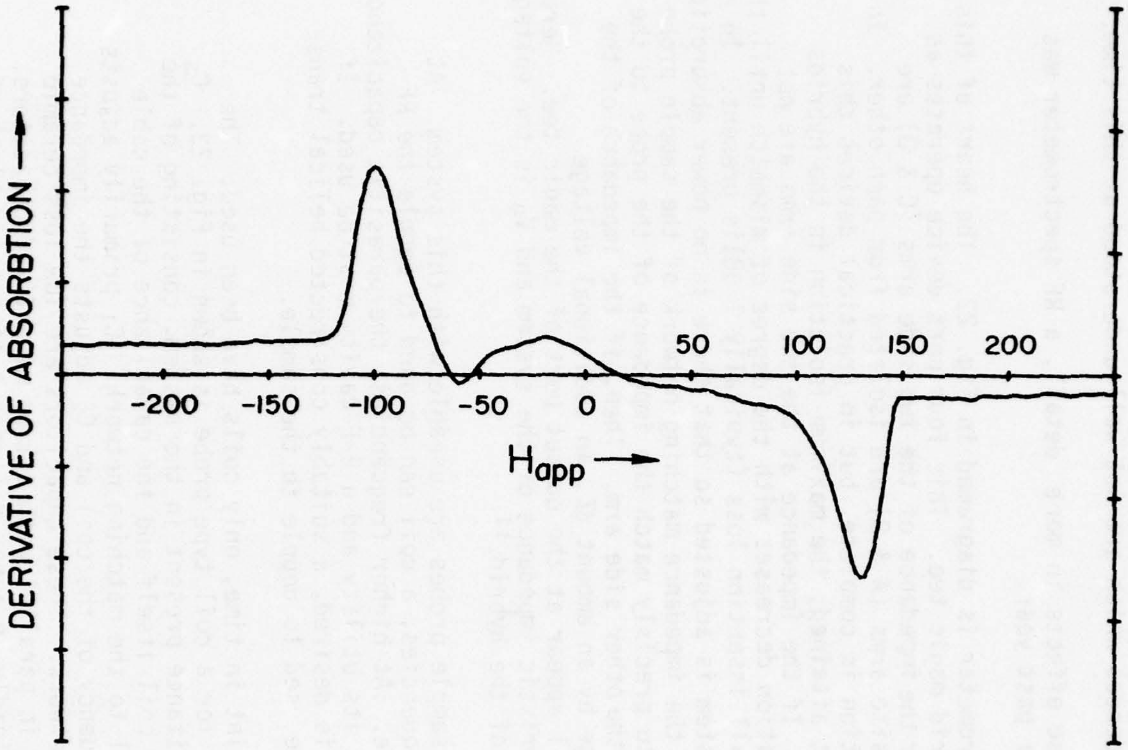

Figure 21. Low field radio frequency signal of a typical magnetic bubble material at 15 MHz.

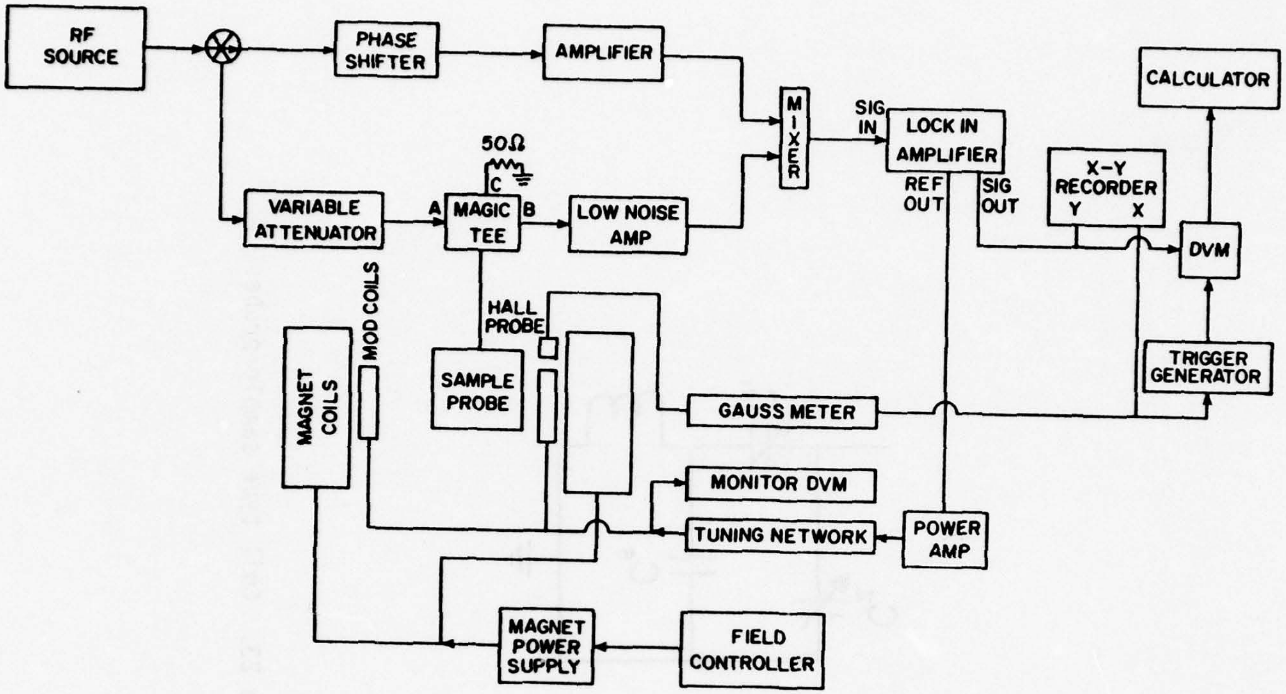

Figure 22. Block diagram of RF spectrometer.

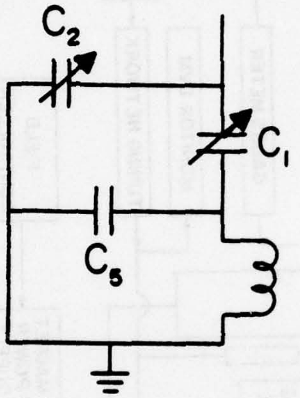

Figure 23. Coil type sample probe.

Using standard circuit theory, the impedance match condition is

$$Z_o/Q\omega L = \left[C_1/(C_1 + C_2)\right]^2 \tag{35}$$

and the resonance condition is

$$C + \frac{C_1C_2}{C_1+C_2} = \frac{1}{\omega^2 L} \tag{36}$$

where Q and L are the Q factor and inductance of the coil respectively. These condition lead to

$$C_1 = (\frac{1}{\omega^2 L} - C)/(1-a)$$

and (37)

$$C_2 = (\frac{1}{\omega^2 L} - C)/a$$

These equations can also be inverted to give

$$L = b/\omega^2$$

and

$$Q = Z_0\ \omega/(\frac{C_1}{C_1+C_2})^2 b \tag{38}$$

where

$$b = C_1 + C_2/(C_1C_2 + C_1C + C_2C)$$

Usual operating procedure to measure L and Q (using a Boonton 260A Q meter), measure C, the capcitance of the probe, (using a ECD model 100 C meter), and use Eq. 37 to calculate the appropriate values for C_1 and C_2. The matching network is then adjusted to these values, using the C meter to verify the values of C_1 and C_2. The system is then powered and a spectrum anylizer is used to monitor the output from the bridge as the frequency is varied. When the frequency of the source matches the tuning of the probe, the power output drops. C_1 and C_2 are now adjusted to tune the probe to the proper frequency and to optimize the impedance match. Once a good match is attained, Eqn. 38 can be used to calculate more exact values for Q and L.

The output signal from the magic tee is amplified and then fed to the double balanced mixer. Since the overall system noise is primarily determined by the noise performance of this amplifier, the use of a low noise amplifier is important. Since the two inputs to the mixer are the same frequency, their difference frequency present at the output port is a DC level proportional to the relative amplitude and phase of the two input signals. The phase shifter in the LO branch allows the observation of either the real or imaginary part of the susceptibility. The bias field is modulated and a lockin amplifier is used to measure the resultant modulated signal at the output of the mixer. The output of the lockin is fed to the Y axis of an X-Y recorder and also to a DVM. The X axis field sweep drive for the X-Y recorder comes from a hall effect gaussmeter whose probe is located as near to the sample as possible. A Typical spectra is shown in Fig. 24.

The use of phase sensitive detection results in the derivitives of the power absorption appearing at the output of the lockin. Since the information desired is the susceptibility, which is proportional to the power absorbed, it is desirable to integrate the signal. This is accomplished by digitizing the signal, storing it in a programable calculator, and then numerically intergrating it. Programs have been written to acquire the data, remove baseline drift, and intergrate the data.

In addition to the RF spectrometer just described, a vibrating sample magnetometer is used to measure the DC susceptibility of the samples. In this instrument, the sample whose moment is to be measured is mounted on a rod and suspended between the pole pieces of the magnet between a pair of pickup coils mounted on the magnet pole pieces, as illustrated in Fig. 25. The other end of the sample rod is connected to a vibrating head mounted above the magnet. When the sample and rod are vibrated, any moment in the sample induces a signal in the pickup coils.

Since the output of the magnetometer is the magnetic moment as a function of field, it is necessary to differentiate this signal to obtain the susceptibility. This is done by digitizing the signal, using the same arrangement used with the RF spectrometer, and numerically smoothing and differentiating the stored data.

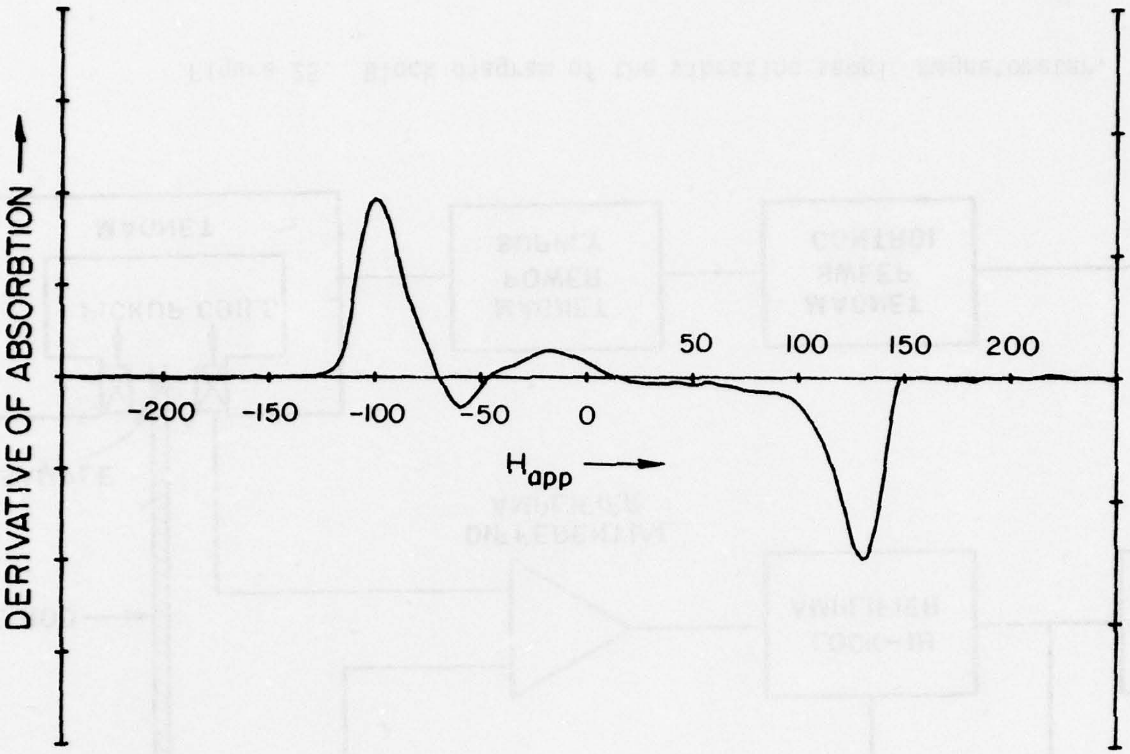

Figure 24. Typical spectrum obtained with the RF spectrometer, showing numerical baseline compensation and integration to obtain susceptibility vs. magnetic field.

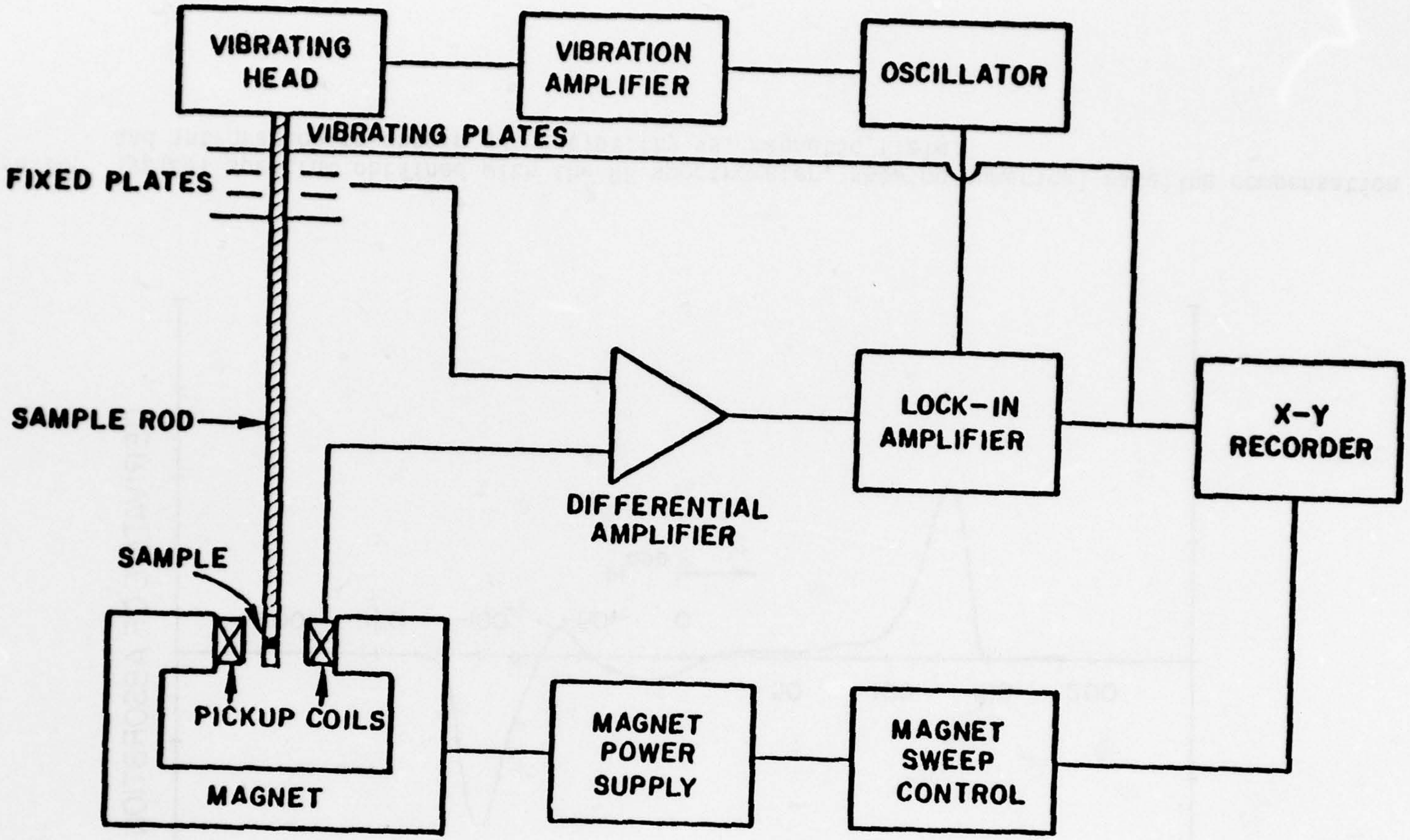

Figure 25. Block diagram of the vibrating sample magnetometer.

Testing Program

The testing program was begun May 23, 1977. Through the period ending December 30, 1977 the majority of the work carried out was directed at setting up facilities, surveying the available literature, and planning directions to be taken in the research.

An engineer was hired (J. Slivinski) in June whose primary responsibility was to set up laboratory and electronic shop facilities to aid in both the materials and testing work. In addition, contacts were made with other groups at Wright Field whose facilities might also be of value in this work (Stu Cummins).

Orders were placed for the various items needed to set up the shop and laboratory. Most of this equipment arrived by the end of September including a TI TRM 0103 92K bubble memory system. Unfortunately this system was not completed by the end of the period due to the slow arrival of some critical components. In addition the design of the memory controller was significantly slowed down due to the resignation of the engineer in August who took a job at a higher salary elsewhere. A Graduate student at OSU (R. Lele) has recently been found to continue this work. He will begin in December. Also the responsibility for help in the electronics shop has been partially filled by another Graduate student (H. Brown) who began work in October.

The main work carried out at OSU during this period involved setting up research directions. A few papers were found which described computer controlled testing facilities for bubble memories. Such systems are quite adequate for small scale memories but for the characterization of very large (10^9 and above) memories the run time becomes quite prohibitive. The obvious difficulty here is the lack of parallel access to the chips. Specifically, if the chip had multiple bubble detectors then the testing time could be reduced by a factor proportional to the number of detectors available. It is just not practical to put several magnitoresistive bubble detectors on a chip, due to the very large areas involved. Because of these and other factors a two step approach was proposed.

There appear to be two major error machanisms in bubble memories. One is due to the faults in the permalloyand conductors overlays and the other is due to faults in the crystalline substrate. Techniques have been described in the literature for detecting faulty crystalline structures. The problem of checking the overlay patterns, however, is not well understood. The proposal here, then, involves techniques for checking this overlay. In general the technique works as follows. An image of the bubble memory overlay pattern is obtained by some means, having resolution adequate to separate the various geometries. The chip is first positioned in the field of view by locating a bench mark in the upper left hand corner and then under computer control, it is oriented and magnified to some pre-specified values. Once this initial positioning and scaling process is completed the chip is scanned left to right, top to bottom. The overlay pattern is checked for errors during this scanning process.

The computer controlled positioning process is fairly straight forward. The magnification is reduced to some low level and the stage (here assume optical imaging via a microscope) is moved in a regular way until the chip is located and then is centered in the field of view. The magnification is increased to near the working value and then a chip edge is located. By tracking the edge a special benchmark may be located and used to set the proper magnification followed by a precise orientation of the chip.

Once the chip is properly positioned, it is possible to move it so that specific areas are within the field of view. A set of metrics are then computed for the given field and compared to a stored known value for that view. If the two sets of numbers are adequately close the chip is moved to a new position and a new comparision is performed. This process continues until the entire chip has been scanned.

The research to be carried out over the next year, then, will involve the following:

(1) A study of the requirements on the system resolution,
(2) Development of the appropriate tracking algorithms,
(3) An examination and comparison of the effacacy of various metrics (such as histograms, moments, etc.), and
(4) An investigation of special purpose computational structures for implementing these algorithms.

The above constitutes a first step in the testing of large scale memories. If a chip is found acceptable via this step it must be electrically characterized. If a chip is found to have faults then no time need be expended on testing it further. In order to perform the electrical characterization in relatively short period of time parallel access to the chip is essential. Such access would be used only for the actual characterization of the device and not for data acquisition in application. One method of attaining this parallel access is illustrated in Fig. 26 and may be described as follows. Polarized laser light is directed into grating A so as to be coupled into the wave guide. The laser light will experience a faraday rotation as it progogates toward the test point. At the test point the laser light is turned toward the surface to the test chip and brought into close proximity of the bubble domain to be tested. (Note the wave guide must be covered with some type of material and lapped so the test point is just under the surface). If the magnitization of the domain is bucking the external magnetic field the effects of the faraday rotation will be decreased. Thus, when the laser light is coupled out of the wave guide at grating B, analyzed and detected it can be determined if there is a magnetic

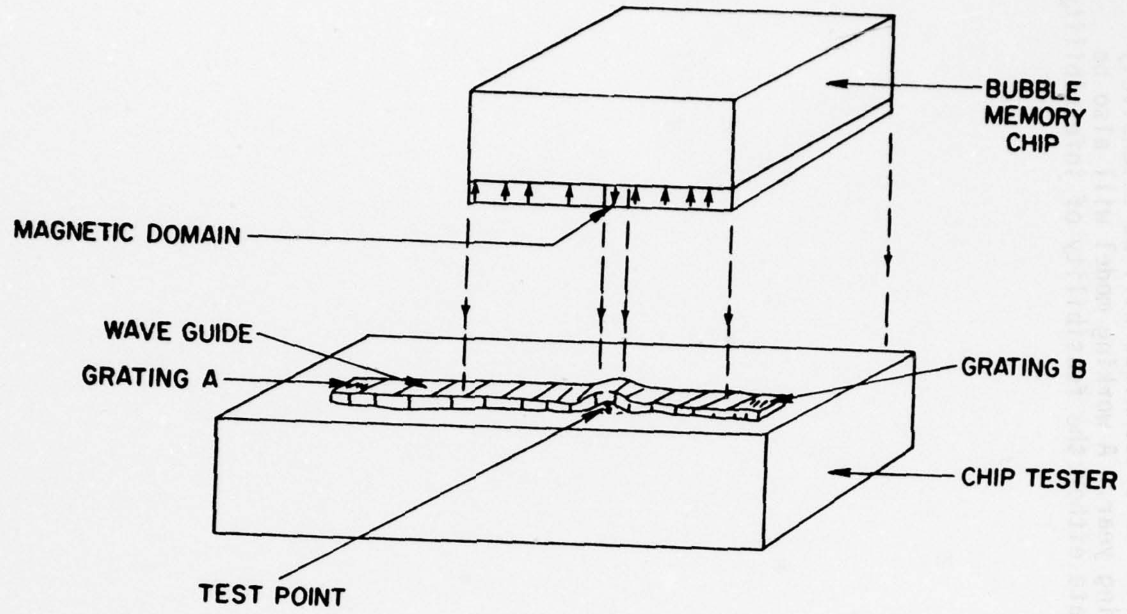

Figure 26. A method of attaining parallel access to a memory chip.

domain at the test point. This technique will be extensively investigated in the coming year. A working model will also be constructed to demonstrate either the feasibility of infeasibility of the basic idea.

APPENDIX

A. HELMHOLTZ COILS

The drive coils used in the M-H looper are of the Helmholtz design. Helmholtz coils consist of two coils arranged such that the distance between the coil planes is equal to the mean radius of the coils. In such an arrangment, the field in the central portion of the median plane is fairly homogenous.

The components of the field between the coils are given by:[12]

$$H_z = \frac{2nI}{R} \Big[0.44959 \left(1 - \frac{b^2}{60R^2}\right) + .0035907 \left(\frac{31b^2 - 3ba^2}{R^2}\right) \frac{r^2}{60R^2} \; X$$

$$(3 \cos^2\theta - 1) - 0.06474 \frac{r^4}{R^4} (35 \cos^4\theta - 30 \cos^2\theta + 3) \Big]$$

and $H_x = \frac{2nI}{10R} \sin\theta \cos\theta \; \Big[-0035967 \left(\frac{31b^2 - 3ba^2}{R^2}\right) \frac{r^2}{R^2} +$

$$06474 \frac{r^4}{R^4} (28 \cos^2\theta - 12) \Big]$$

The definition of r and θ and the coordinate axes are defined in Fig. A1. I is in amps, n is the no. of turns in each coil. R,a,b, and r are in cm. In the median plane between the coil, $\theta = \pi/2$. In this case;

$H_x = 0 \; (H_y = 0)$

$$H_z = \frac{2nI}{R} \Big[.44959 \left(1 - \frac{b^2}{60R^2}\right) - .0035967 \left(\frac{31b^2 - 36a^2}{R^2}\right) \frac{r^2}{R^2}$$

$$-3(.06474) \frac{r^4}{R^4} \Big] .$$

This equation assumes that the current is distributed uniformly over the crosssection a,b. Figures A2 and A3 are a listing and typical output of a program (for a H-P 9820 calculator) to plot the magnititude of the field in the median plane. The coordinate r represents the distance from the central point in the median plane. H_{max} is the value of the field at the center. The program calculated that for these dimensions, $H/H_{max} = .99$ when $r = 2.83$ cm. Theorectically with these dimensions, the field should be homogenous to 1% over about

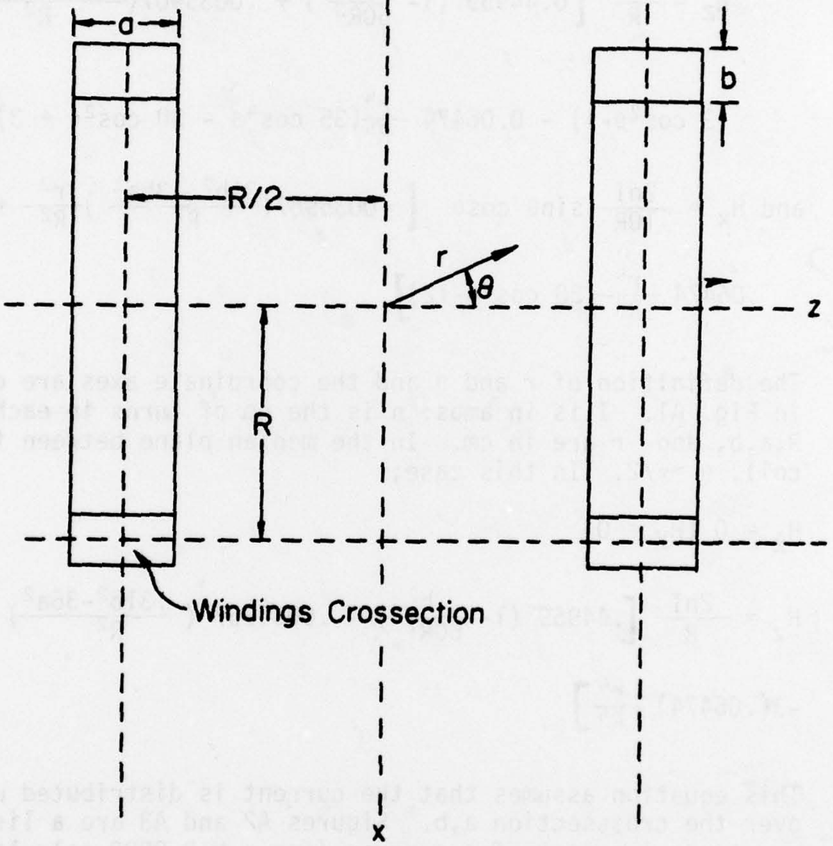

Figure A-1. Geometry of drive coils constructed for the M-H looper.

```
0:
PRT "H IN MEDIAN
";PRT "PLANE BET
. TWO";PRT "HELM
. COILS."⊢
1:
PRT "H IN GAUSS"
;PRT "R IN CM.";
SPC 2⊢
2:
ENT "COIL RA. (C
M)",R0,"TURNS EA
.",R1⊢
3:
ENT "A",A,"B",B⊢
4:
ENT "CURRENT (AM
PS)",R5⊢
5:
PRT "COIL RA.= (
CM)";PRT R0;SPC
1;PRT "TURNS EA.
 ="⊢
6:
PRT R1;SPC 1;
PRT "A= (CM)";
PRT A;SPC 1⊢
7:
PRT "B= (CM)";
PRT B;SPC 1;PRT
"I= (AMPS)";PRT
R5;SPC 2⊢
8:
.44959(1-B↑2/60R
0↑2)→R2⊢
9:
.0035967((.31B↑2
-36A↑2)/R0↑4)→R3
⊢
10:
3*.06474/R0↑4→R4
⊢
11:
0→X:(2R1R5/R0)(R
2-R3*X↑2-R4X↑4)→
R6⊢
12:
PRT "HMAX= (OE.)
";PRT R6;SPC 1;
PRT "R=";PRT "-3
 TU +3 CM.";SPC
2⊢
```

```
13:
SCL -3,3,0,R6+.2
R6⊢
14:
ENT "AXES?(1=Y,2
=NO)",R7⊢
15:
IF R7>1;GTO +2⊢
16:
AXE (0,0,.1,R6/2
0)⊢
17:
-3→X⊢
18:
(2R1R5/R0)(R2-R3
X↑2-R4X↑4)→Y⊢
19:
PLT X,Y;X+6/100→
X⊢
20:
IF X≤3;GTO -2⊢
21:
PEN ;0→X⊢
22:
(2R1R5/R0)(R2-R3
X↑2-R4X↑4)→Y⊢
23:
IF Y/R6≤.99;JMP
2⊢
24:
X+3/500→X;GTO -2
⊢
25:
PRT "H/HMAX≤.99"
;PRT "AT R= (CM)
";PRT X;SPC 10⊢
26:
STP ⊢
R309
```

```
H IN MEDIAN
PLANE BET. TWO
HELM. COILS.
H IN GAUSS
R IN CM.


COIL RA.= (CM)
 6.000000000E 00

TURNS EA. =
 3.000000000E 02

A= (CM)
 2.540000000E 00

B= (CM)
 3.810000000E 00

I= (AMPS)
 2.000000000E 01


HMAX= (OE.)
 8.931371357E 02

R=
-3 TO +3 CM.


H/HMAX≤.99
AT R= (CM)
 2.826000000E, 00
```

Figure A-2. Program for HP 9820 calculator used to calculate the magnetic field of the M-H looper drive coils.

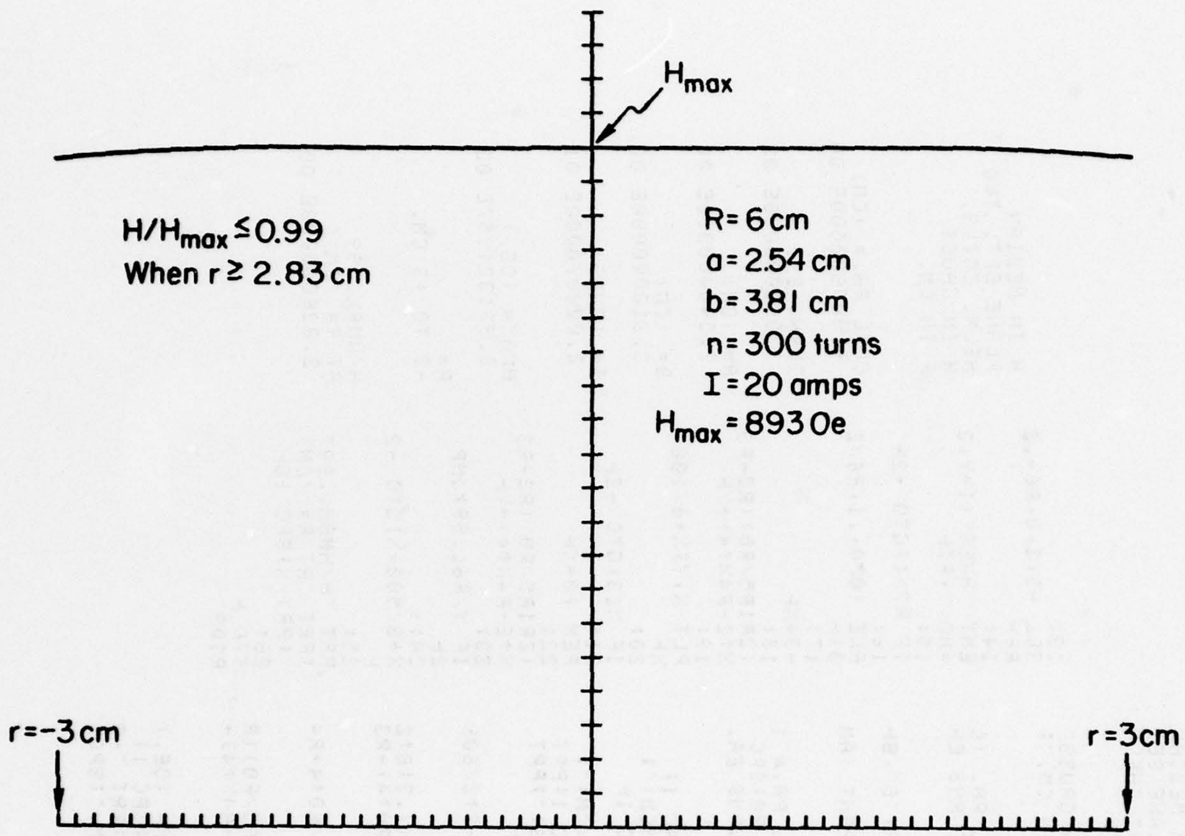

Figure A-3. A plot of the magnetic field in the median plane.

a 2 inch diameter circle. The dimensions used in this calculation were those used for the final coils.

B. Magnetic Field Due to a Uniformly Magnetized Thin Film.

The relationship between the magnetization of the sample M, and the sample magnetic field, H_S is now discussed. The field due to a volume of magnetization V, external to that volume, is given by:

$$\vec{H} = \int_S \frac{\vec{M}\cdot\vec{ds}}{r^2}\ \hat{r} - \int_V \frac{\vec{\nabla}\cdot\vec{M}}{r^2}\ dV\ \hat{r}$$

The first intergral is over the boundary surface of the volume. $\vec{M}$ is the volume's specially varying magnetization, r is the distance from the point of intergration to the point where $\vec{H}$ is being evaluated, and $\hat{r}$ is a unit vector from the point of integration to the point of evaluation. The volume for a thin film is shown in Fig. A4. The point of evaluation is assumed to be close enough to the plate that z << radius of the plate. The plate is assumed to be uniformly magnetized and the ends of the plate are assumed to be far enough away that their contributions can be neglected. Since $\nabla\cdot M \equiv 0$, the field is given by

$$H_S = \int_{s_1} \frac{MdA\hat{r}}{r^2} - \int_{s_2} \frac{MdA\hat{r}}{r^2}$$

The integral over s_1 is performed first. To facilitate the integration, the integral is broken up into concentric rings of thickness dx. This is illustrated in Fig. A5. The field due to all portions of a particular ring is given by

$$d\,H_{S_1 z} = \frac{MdA}{r^2}\cos\theta$$

The planar components from all section of a ring add to zero. For a ring;

$$dA = 2\pi x dx$$

$$\cos\theta = \frac{z}{(z^2+x^2)^{1/2}}$$

$$dH_z = \frac{Mz\ 2\pi x dx}{(z^2+x^2)^{3/2}}$$

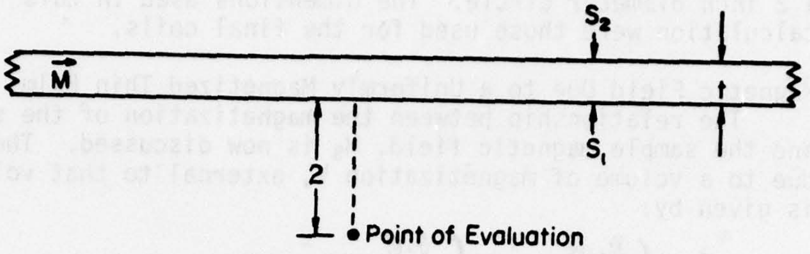

Figure A-4. A cross section of a thin film and the definition of parameters used in the text.

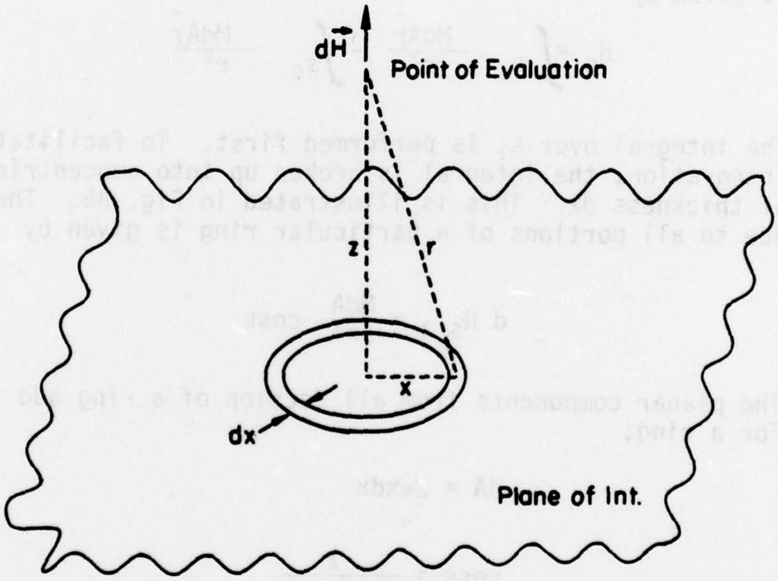

Figure A-5. The element of integration of the thin film and the definition of parameters used in the text.

and

$$H_{s_1z} = \int_0^{\infty} \frac{Mz\, 2\pi x dx}{(z^2+x^2)^{3/2}}$$

letting

$$u \equiv z^2 + x^2$$

$$du = 2xdx$$

and

$$H_{s_1z} = \int_{z^2}^{\infty} \frac{zM\pi du}{u^{3/2}}$$

$$= 2zM\pi \left[U^{-\frac{1}{2}}\right]_{\infty}^{z^2}$$

$$H_{s_1z} = + \frac{2\pi M}{z}$$

Simularly, the surface S_2 can be evaluated.

$$H_{s_2z} = \frac{-2\pi M}{(z+t)}$$

The total field is given by:

$$H_z = 2\pi M \quad \frac{t}{(z+t)(z)}$$

For z >> t (practical placement of the pickup coil demands this)

$$H_z \simeq \frac{2\pi Mt}{z^2} \qquad \text{(Oe.)}$$

IC. Expected Signal Strength

In this section the relative sizes of the emf's induced in the pickup coil are estimated. First the sample signal. It is assumed for simplicity, that M varies sinosoidally as does the the drive field. The pickup coil is assumed to be 2 mm from the sample, have 100 turns and a radius of 2mm. Also assume that,

$$4\pi M = 400 \text{ gauss}$$

$$t = 5 \times 10^{-4} m$$

$$f = 200 \text{ Hz}$$

$$V_s = \frac{d}{dt} \frac{N}{C} \int_A H \cdot ds$$

$$H = \frac{t\, 2\pi\, M}{z^2}$$

$$2\pi M = 200 \sin (2\pi f t)$$

$$V_s = \frac{N}{C} \frac{t}{z^2} 200\, (2\pi f) \cos (2\pi f t) \cdot (\pi r^2)$$

When

$$\cos 2\pi f t = 1$$

$$V_s \sim 1.3 \times 10^{-6} \text{ Stat V}$$

$$= 400\ \mu V$$

The potential due to the drive field is now calculated. For a 400 gauss, peak A.C. field at 200 Hz

$$H = 400 \sin 2\pi f t$$

$$V_d = \frac{N}{C} 400\omega\, (\pi r^2) (\cos \omega t = 1)$$

The ratio of $V_d/V_s \equiv 1.6 \times 10^2$.

References

1. C. Kooy and U. Enz; "Experimental and Theoretical Study of the Domain Configuration in Thin Layers of $BaFe_{12}O_{19}$", Philips Res. Repts. 15, 7(1960).

2. C. W. Searle (private communication).

3. A. A. Theile; "The Theory of Cylindrical Magnetic Domains", Bell Syst. Tech. J. 48, 3287(1969) and "Theory of the Static Stability of Cylindrical Domains in Uniaxial Platelets", J. Appl. Phys.

4. I. Maartense, C. W. Searle and M. G. Mier; "Bubble Film Characterization by AC Susceptibility Measurements", J. Appl. Phys. 49, 1882(1978).

5. S. Chikazumi; "Physics of Magnetism", John Wiley and Sons, 1964, Chapter 2.

6. J. C. Huber; "Compensation Bridge for Hysteresis Loop Tracers", Rev. Sci. Inst. 41, 882(1970).

7. M. G. Mier, H.W.S. Swenson and P. E. Wigen; "Microwave Measurement of Magnetic Bubble Collapse and Stripout Field", AIP Conf. Proc. 34, 178(1976).

8. P. E. Wigen, A. A. Parker, P. S. Limaye and S. C. Hart; "Spinwave Scattering from Magnetic Domain Walls", Bull. ASP 23, (1978).

9. A. A. Parker, P. E. Wigen and M. G. Meir; Appl. Phys. Letters, "Spinwave Scattering from Magnetic Domain Walls", (to be published).

10. P. E. Wigen, "Magnetic Excitations", Lectures at the Enrico Fermi Summer School of Physics, Varenna, Italy, July 1977 (to be published).

11. T. S. Stakelon; Nuclear Magnetic Resonance in Single Crystals of the Dilute Magnetic Alloys: CuFe, CuCO, and CuNi, Thesis, University of Illinois, 1975.

12. A. E. Ruark and M. F. Peters; "Helmholtz Coils for Producing Uniform Magnetic Fields", J. Opt. Soc. Am., 13, 205(1926).

☆U.S.Government Printing Office: 1978 — 757-080/8